THESIS

THE UNCONVENTIONAL EYEWALL REPLACEMENT CYCLE OF HURRICANE OPHELIA (2005)

Submitted by

Muhammad Naufal Bin Razin

Department of Atmospheric Science

In partial fulfillment of the requirements

For the Degree of Master of Science

Colorado State University

Fort Collins, Colorado

Spring 2018

Master's Committee:

Advisor: Michael M. Bell

Kristen L. Rasmussen
Wolfgang Bangerth

Copyright by Muhammad Naufal Bin Razin 2018

All Rights Reserved

ABSTRACT

THE UNCONVENTIONAL EYEWALL REPLACEMENT CYCLE OF HURRICANE OPHELIA (2005)

One of the mechanisms proposed for the spin-up of the tropical cyclone (TC) mean tangential circulation is the convergence of absolute angular momentum above the boundary layer. This mechanism is important for the outer primary circulation and results in the broadening of the TC wind field. We hypothesize that the mid-level inflow associated with the stratiform precipitation in TC rainbands may be instrumental in spinning up the broader circulation, and may be important in the development of secondary eyewalls. Hurricane Ophelia (2005) underwent an unconventional eyewall replacement cycle (ERC) as it was a Category 1 storm located over cold sea surface temperatures near 23°C. The ERC was observed using airborne radar observations during the Hurricane Rainband and Intensity Change Experiment (RAINEX). Data was collected from the single-parabolic X-band radar aboard the National Oceanic and Atmospheric Administration (NOAA) P-3 aircraft and from the dual-beam X-band Electra Doppler Radar (ELDORA) aboard the Naval Research Laboratory (NRL) P-3 aircraft. The two aircraft flew simultaneously along Ophelia's primary rainband during a research flight beginning around 1700 UTC on 11 September 2005, allowing for quad-Doppler wind retrievals along the rainband. Analyses were conducted using a spline-based three-dimensional variational wind synthesis technique. Results showed a broadened tangential wind field associated with the ERC was observed in the stratiform-dominant rainbands of Ophelia. The broadening of the tangential wind field was collocated with the strongest radial advection of angular momentum through the stratiform mid-level inflow and is consistent with the proposed mechanism for TC intensity change.

ACKNOWLEDGMENTS

I owe my deepest gratitude to my advisor Professor Michael Bell for taking me on as his graduate student when all the doors seemed to have closed on me, and for allowing me the opportunity to pursue my passion in tropical meteorology. His constant reminder on the importance of advancing the science for the betterment of society has always served as a source of motivation. This thesis would not have been possible without his unending support, wisdom, patience in his guidance, and his words of encouragement that seemed to have always come when I needed them most.

I would like to thank my committee members, Professor Kristen Rasmussen and Professor Wolfgang Bangerth for their constructive criticisms, comments, and critique in guiding the completion of this thesis.

I would like to express a great deal of gratitude to my grandfather Omar bin Md Khir, without whom my adventure in the United States would not have been possible.

I am indebted to Dillon Dodson, and the past and present members of the Bell research group, particularly Annette Foerster, Jonathan Martinez, Ellie Delap, Ben Trabing and Ting-Yu Cha for their help in all things programming, for being a great place to bounce off ideas, for an awesome office environment, and for helping me through multiple coding-related meltdowns.

I would like to show my gratitude to my mother Aniza Khir binti Omar, my three sisters, and fellow friends for their continued moral support.

This research was supported by the National Science Foundation CAREER Award AGS-1701225.

This thesis is typeset in LaTeX using a document class created by Leif Anderson and modified by Christopher Slocum.

TABLE OF CONTENTS

Abstract ii

Acknowledgments iii

List of Figures v

Chapter 1. Introduction 1

Chapter 2. Data & Methods 9

2.1 RAINEX & Airborne Radar Data 9

2.2 Best Track, SHIPS, GRIDSAT & OISST 14

2.3 Flight-Level Dataset & Satellite Microwave Imagery 15

2.4 Analysis 17

Chapter 3. Results 18

3.1 Hurricane Ophelia (2005) 18

3.2 Flight-Level Tangential Wind Evolution 20

3.3 Rainband Analysis 25

3.4 Absolute Angular Momentum (AAM) Budget 41

Chapter 4. Conclusion 47

References 49

LIST OF FIGURES

Fig. 2.1 Flight Tracks 10
Fig. 2.2 DBZ Difference Distribution 11
Fig. 2.3 z Difference Distribution 12
Fig. 2.4 Reflectivity Correction Comparison 13
Fig. 2.5 Dual-Doppler vs Quad-Doppler Comparison 14

Fig. 3.1 Storm Track 19
Fig. 3.2 Storm Intensity 20
Fig. 3.3 Environmental Shear 21
Fig. 3.4 Sea Surface Temperatures 22
Fig. 3.5 Flight-Level Tangential Wind Evolution 22
Fig. 3.6 Eyewall Replacement Cycle Satellite Microwave Imagery 23
Fig. 3.7 Integrated Kinetic Energy 25
Fig. 3.8 1853 UTC Leg Top-Down View 26
Fig. 3.9 1853 UTC Leg Azimuthally-Averaged Cross-Section 27
Fig. 3.10 1853 UTC Leg CFAD 29
Fig. 3.11 2018 UTC Leg Top-Down View 31
Fig. 3.12 2018 UTC Leg Azimuthally-Averaged Cross-Section 33
Fig. 3.13 Datapoint Fraction 34
Fig. 3.14 2018 UTC Leg Individual Cross-Sections 35
Fig. 3.15 2133 UTC Leg Top-Down View 36
Fig. 3.16 2133 UTC Leg Azimuthally-Averaged Cross-Section 37
Fig. 3.17 2133 UTC Leg Individual Cross-Sections 38
Fig. 3.18 2154 UTC Leg Top-Down View 40
Fig. 3.19 2154 UTC Leg Azimuthally-Averaged Cross-Section 41
Fig. 3.20 Research Flight Satellite Microwave Imagery 42
Fig. 3.21 1853 UTC Momentum Budget 43
Fig. 3.22 2018 UTC Momentum Budget 44
Fig. 3.23 2133 UTC Momentum Budget 45
Fig. 3.24 2154 UTC Momentum Budget 46

CHAPTER 1

INTRODUCTION

High impact weather such as tropical cyclones (TC) have the potential to cause massive loss of life and inflict tremendous damage to infrastructure and national economy, particularly in low-income nations. The ability to better forecast TCs will undoubtedly help reduce their impacts by improving the lead time for governments to implement emergency procedures prior to a TC landfall. Over the past 20 years, significant improvements have been made in TC forecasts, with notable strides made particularly in TC track forecasts. While there has also been more modest yet statistically significant improvements in TC intensity forecasts, the improvements in short-term (24-hour forecast period) TC intensity forecasts have been marginal (DeMaria et al. 2014).

For TCs that occur in the western hemisphere, the Saffir-Simpson Hurricane Wind Scale is used to classify TC intensity. The Saffir-Simpson Hurricane Wind Scale classifies TC intensity according to the strength of the maximum sustained 1-minute tangential wind speed at 10 meters above the ocean surface. While there are various definitions for TC size, a commonly used metric is the radius of gale-force (17 m s^{-1}) or hurricane-force (33 m s^{-1}) winds relative to the TC center (Smith et al. 2009), where the radius of either of these wind thresholds is proportional to the TC size. TC intensity determines the magnitude of the damage to the infrastructure in the TC path, whereas TC size determines the size of the damage swath corresponding to the TC intensity. While there is no direct correlation between TC intensity and TC size, their evolution typically coincide during an eyewall replacement cycle (ERC), a phenomenon in which a TC undergoes an increase in size, but temporarily weakens before it re-intensifies. This phenomenon is commonly observed in major TCs (Category 3 or above).

Hurricane Ophelia (2005), the subject of this study, underwent an unconventional ERC, as it was a weak Category 1 storm located over cool sea surface temperatures (SSTs). The SSTs were approximately three degrees Celsius below what is generally understood to be the threshold of 26.5°C needed for TC genesis and sustenance (Dare and McBride 2011). Using airborne radar observations of Hurricane Ophelia from the Hurricane Rainband and Intensity Change Experiment (RAINEX) field campaign, the broadening of Ophelia's tangential wind field - thus the expansion of its size - associated with the ERC was observed in the stratiform-dominant portion of its rainbands. This suggests that the stratiform-dominant portion of Ophelia's rainbands played an influential role in the ERC by broadening the TC

tangential wind field, most likely through strong convergence of absolute angular momentum associated with the stratiform mid-level inflow. While the proposed role of rainband stratiform precipitation as a mechanism to broaden the TC wind field is relatively new in the literature (Didlake and Houze 2013b), the role of angular momentum convergence through non-stratiform processes in the spin-up of TCs has been well established.

Smith et al. (2009) proposed two mechanisms that may lead to the spin-up of the TC mean tangential wind field. The first mechanism involves the radial convergence of absolute angular momentum M above the boundary layer, where M is materially conserved in the absence of friction. This is achieved by the inward advection of high absolute angular momentum air through weak radial inflow in the middle troposphere, in response to middle-to-upper tropospheric heating in the region immediately outside of the TC inner core (Fudeyasu and Wang 2011). This mechanism is associated with the spin-up of the TC outer core tangential winds, which broadens the TC wind field and increases the TC size.

The second mechanism involves the radial convergence of absolute angular momentum M within the boundary layer, and is influential in the spin-up of the TC inner core. This is achieved when the angular momentum gained through the inward radial advection of high angular momentum air is larger than the loss of angular momentum to the surface through friction (Smith et al. 2009). Of interest to this particular study is the first mechanism. While Smith et al. (2009) did not frame their results in the context of an eyewall replacement cycle (ERC), the first mechanism may play a role in broadening the TC wind field prior to an ERC through the rainband stratiform mid-level inflow.

Using flight-level data from aircraft reconnaissance missions that observed 24 ERC events in 14 TCs from 1984 to 2007, and complemented by the corresponding satellite microwave imagery, Sitkowski et al. (2011) compiled a climatology of the tangential wind evolution associated with ERCs. They classified ERC events into three phases: intensification, weakening, and re-intensification. A secondary tangential wind maximum was first observed in the TC outer core during the intensification phase. This was followed by the contraction of the radius of maximum tangential wind speed both in the TC inner core (primary wind maximum) and outer core (secondary wind maximum). The intensification phase is followed by the weakening phase. This phase was associated with the weakening of the primary wind maximum as the secondary wind maximum continued to contract, and ended when the secondary wind maximum intensity surpassed the primary wind maximum intensity.

The re-intensification phase was marked by the continued weakening of the old primary wind maximum as the secondary wind maximum became the new primary wind maximum. This tangential

wind evolution was accompanied by i) the formation and contraction of a secondary eyewall associated with the strengthening and contraction of the secondary wind maximum, and ii) the dissipation of the primary eyewall associated with the dissipation of the primary wind maximum. As these two processes overlap, they may form concentric rings of convection (concentric eyewalls) that can easily be distinguished in satellite microwave imagery. However, Sitkowski et al. (2011) noted that the presence of the secondary wind maximum always preceded the observation of concentric eyewalls in the satellite microwave imagery.

ERCs are known to occur in mostly major tropical cyclones (Category 3 or stronger on the Saffir-Simpson Hurricane Wind Scale). While ERCs are not fully understood, the broadening of the TC tangential wind field associated with an ERC bears strong resemblance to the broadening of the TC tangential wind field associated with the first mechanism proposed by Smith et al. (2009). The location where the secondary tangential wind maximum occurs prior to an ERC suggests that TC rainbands, located outside of the TC inner core, may provide a method through which the first mechanism could occur. Therefore, understanding the dynamics of TC rainbands may be crucial in understanding the processes behind ERCs.

TC rainbands consist of an arrangement of convective and stratiform precipitation. Understanding the differences between both types of precipitation is crucial in understanding how they influence rainband structure. These fundamental differences were discussed in Houze (1997). Convective precipitation is characterized by a net upward mass transport with net latent heating at all vertical levels. Mass continuity dictates that the net upward mass transport must be accompanied by a net horizontal convergence at low levels and a net horizontal divergence at upper levels. The strong updrafts associated with the convection condense water vapor rapidly and precipitation particles grow predominantly through collection; that is, coalescence for water droplets and riming for ice particles. The strong updrafts also keep the precipitation particles aloft for longer periods before they grow large and heavy enough to overcome the updrafts and fall out as heavy precipitation. Therefore, in a horizontal cross-section of radar reflectivity, convective precipitation appears as distinct cells of heavy precipitation.

In the tropics, stratiform precipitation occurs predominantly from the decay of convective precipitation. Stratiform precipitation is characterized by net latent heating and net upward mass transport in the mid-to-upper levels, and latent cooling and net downward mass transport in the lower levels. Through mass continuity, the vertical divergence profile of stratiform precipitation has divergence in the lower and upper levels, and convergence in the mid-levels. The net upward mass transport in the

mid- to upper levels is generally too weak to keep the precipitation particles aloft long enough for them to grow through collection. Rather, the main growth mechanism for precipitation particles in stratiform precipitation is vapor deposition. Near the freezing/melting level, the surfaces of ice particles begin to melt, allowing them to stick together to form large aggregates that are covered in a layer of meltwater and forming the melting layer. Just below this level, fully melted precipitation particles fall out of the melting layer at faster downward velocities relative to the ice particles in the melting layer. The weak vertical velocities, higher dielectric constant of water, and distribution of the different precipitation types and sizes in and near the melting layer combine to produce a uniformly layered structure with a "brightband" near the melting level, as commonly observed in a vertical cross-section of radar reflectivity. However, the brightband is an artifact of the radar. The absence of a radar brightband does not mean that the precipitation is not of the stratiform type.

The precipitation structure of a TC rainband complex was first detailed by Willoughby et al. (1984) and later updated by Houze (2010). In contrast to the quasi-circular geometry of the eyewall, the rainband complex consists of an aggregation of convective and stratiform precipitation that takes on a spiral geometry, sometimes connected to the eyewall through a connecting band. The rainband complex can be further subdivided into three categories: the distant rainbands, the principal rainband, and the secondary rainbands. Distant rainbands are deep buoyant convective elements located far from the center of the storm ($>$ 200 km), along the confluence line between the low-level cyclonic TC wind field and the low-level larger-scale flow.

The principal rainband is the most prominent feature of all the rainbands and is quasi-stationary relative to the translating storm center. The upwind portion of this rainband consists of mostly convective precipitation. Ice particles ejected from collapsing convection are advected downwind and form stratiform precipitation there, where it is nearly tangent to the eyewall. The progression from the convective precipitation upwind to the stratiform precipitation downwind resembles that of the life cycle of convective precipitation in the tropics. Given that much of the principal rainband lies within the inner region of the TC, it is constrained by vortex dynamics whereby the vertical extent of the embedded convective cells are confined by the upper-level outflow from the eyewall (Hence and Houze 2012). Moreover, unlike convective cells in distant rainbands that are more vertically upright, the convective cells in the inner regions of TCs are tilted radially outward with height in a similar fashion to convective cells in the eyewall (Barnes et al. 1983). The origin of the principal rainband is not fully understood.

Secondary rainbands can be found radially inward of the principal rainband, but tend to be smaller and are more transient compared to the principal rainband. In addition to the textbook structure of TC rainbands as illustrated by Houze (2010), the distribution of precipitation in TC rainbands are also influenced by the large-scale environment around the storm. Through a statistical analysis of Tropical Rainfall Measuring Mission Precipitation Radar (TRMM PR) three-dimensional reflectivity data, Hence and Houze (2012) found that the vertical shear of the horizontal wind in the large-scale environment of a TC has a strong influence on the azimuthal distribution of precipitation in its rainband. Convective precipitation is prominent in the right-of-shear quadrants while stratiform precipitation is prominent in the left-of-shear quadrants.

Barnes et al. (1983) were the first to utilize observational data to shine a light on the kinematic structure of TC rainbands. They used flight-level data along with radar reflectivity data from two National Oceanic and Atmospheric Administration (NOAA) P-3 aircraft that flew in a cross-band flight routine at various altitudes in Hurricane Floyd (1981). Observations using their low-resolution dataset were later validated by the higher resolution datasets obtained in the Hurricane Rainband and Intensity Change Experiment (RAINEX, Houze et al. 2006). Using dual-Doppler observations from the National Center for Atmospheric Research (NCAR) Electra Doppler Radar (ELDORA) aboard the Naval Research Laboratory (NRL) P-3 aircraft that flew along TC rainbands during RAINEX, the kinematic structures of the convective and stratiform precipitation in Hurricanes Rita and Katrina were analyzed by Hence and Houze (2008), Didlake and Houze (2009), and Didlake and Houze (2013a,b).

The kinematic structure of the upwind convective portion of the principal rainband was illustrated by Hence and Houze (2008) and Didlake and Houze (2009). There are three distinct convective-scale trajectories that are evident in the radial cross-section of the upwind convective portion of the rainband. The first is the secondary circulation characterized by a low-level radial inflow that turns upward at the base, and outward near the top of the convective cell. A maximum positive vertical vorticity anomaly can be found in the updraft core of the convective cell and is associated with a tangential wind maximum located radially outside of the convective cell. This tangential wind maximum is a convective-scale phenomenon termed the secondary horizontal wind maximum (SHWM) by Samsury and Zipser (1995), and can be found anywhere in the low to mid-levels. The vertical extent of the height of the convective cells and its SHWM decreases with decreasing distance from the center of the storm (Didlake and Houze 2013a).

An idealized modeling study by Moon and Nolan (2010) showed that the secondary circulation is the response of a hurricane wind field to the convective heating within the spiral rainband, and that the SHWM arises from the conservation of angular momentum of the radial inflow. The convective scale secondary circulation helps to intensify the SHWM by advecting more positive vertical vorticity into the updraft core through the tilting of horizontal vorticity generated by vertical shear of the horizontal wind directly underneath the SHWM, and vortex stretching from the convergence at the base of the convective cell (Hence and Houze 2008). The second trajectory is a low-level downdraft that originates from radially outside of the convective cell and subsides at the base of the convective core. This low-level downdraft was noted by Barnes et al. (1983) and is thought to be forced by precipitation drag (Didlake and Houze 2009).

The third trajectory is an inner-edge downdraft (IED) that occurs radially inward of the convective cell. The IED is caused by buoyancy-induced pressure gradient acceleration (BPGA) from a radially-adjacent, upwind, or downwind buoyant updraft. The combination of forcing by dynamic pressure perturbation and evaporative cooling of adjacent heavy precipitation of the rainband allows the downdraft to reach the surface, and creates a strong reflectivity gradient radially inward of the convective cell. Just as there is a positive vertical vorticity anomaly in the updraft core of the convective cell associated with the tilting of horizontal vorticity generated by vertical shear of the horizontal wind directly underneath the SHWM, there exists a negative vorticity anomaly radially inward of the convective cell. The IED advects this negative vertical vorticity anomaly downward as it converges in the lower levels. The presence of this negative vertical vorticity anomaly produces another tangential wind maximum on its radially inward side, known as the low-level wind maximum (LLWM, Didlake and Houze 2009).

There are several theories as to how the kinematic structure of the upwind convective portion of the rainband may affect TC intensity. Barnes et al. (1983), and Hence and Houze (2008) hypothesized that the low-level downdrafts transport low moist static energy air towards the center of the storm and therefore weakens it. Simultaneously, Hence and Houze (2008) also hypothesized that the strengthening of the SHWM may make the rainband more robust and, through vortex Rossby wave dynamics elucidated by Montgomery and Kallenbach (1997), may help to form a secondary eyewall. Didlake and Houze (2009) postulated that the inward advection of the LLWM by low-level radial inflow may help intensify the storm by increasing the tangential winds closer to its center through the conservation of angular momentum.

The downwind stratiform portion of the rainband of Hurricane Rita was analyzed by Didlake and Houze (2013b). The upwind segment of the larger downwind stratiform portion of the rainband is characterized by a kinematic structure similar to that of a typical stratiform precipitation. In the lower levels, the vortex-scale circulation induces boundary layer inflow and supergradient outflow. Remnant net upward mass transport and latent heating from the upwind convective portion of the rainband occur in the upper levels. The upward vertical motion travels radially outward along lines of constant angular momentum. The rising outflow forms a sloping cloud base near the outer edge of the precipitation band, beneath which falling ice particles induce sublimational cooling that subsequently produces a deep mid-level inflow burst through the generation of horizontal vorticity that arises from the radial gradient of buoyancy.

Radially-inward of the inflow burst, near the brightband, a similar process involving cooling due to the melting of precipitation induces another inflow burst. A local convergence maximum occurs radially inward of the second inflow burst, where air may flow upward and outward, forming a secondary circulation similar to that seen in convective precipitation, or downward and inward, forming a downdraft that continues towards the center of the storm. The upward motion above the local convergence maximum promotes the growth of larger precipitation particles, and a zone of enhanced reflectivity corresponding to enhanced precipitation can be found beneath this convergence maximum.

The kinematic structure evolves into a completely different structure in the downwind segment of the larger downwind stratiform portion of the rainband, while still maintaining a similar precipitation structure. The downwind segment of the stratiform precipitation is characterized by predominant outflow across all vertical levels, disorganized vertical motions, the absence of the zone of enhanced precipitation, and the presence of a mid-level tangential jet. This tangential jet is of a different origin compared to that of the SWHM found in the upwind convective portion of the rainband. The SHWM is induced by convective-scale motions and can occur anywhere in the lower to mid-levels (Didlake and Houze 2013a), whereas the tangential jets that occur in stratiform precipitation are a part of the larger mesoscale motion and occur consistently in the mid-levels. A momentum budget analysis concluded that this tangential jet is formed through the advection of momentum in the upwind segment of the stratiform portion of the rainband (Didlake and Houze 2013b).

Didlake and Houze (2013b) proposed two ways in which the downwind stratiform portion of the rainband may affect the intensity of a TC. The descending mid-level inflow may advect dry mid-level air closer towards the center of the storm, where it could be ingested into the eyewall through turbulent

mixing. The heat content of the eyewall is thus diluted, contributing to the weakening of the storm. This process is similar to the low-level downdrafts in the upwind convective portion of the rainband. However, the persistent mid-level inflow advects angular momentum inward, strengthening the local tangential winds and resulting in the expansion of the axisymmetric TC wind field - a process akin to the first mechanism proposed by Smith et al. (2009). The expansion of the TC wind field may subsequently lead to the secondary eyewall formation and the strengthening of the storm intensity. Didlake and Houze (2013b) also argued that given the prominent areal extent of the downwind stratiform portion of the rainband and its closer proximity to the center of the storm compared to the more discrete convective cells farther out, the downwind stratiform portion of the rainband is more efficient at increasing the intensity of the storm.

Guided by the findings of these studies, the role of rainband stratiform precipitation in the ERC of Hurricane Ophelia (2005) was investigated using RAINEX airborne radar dataset and a spline-based three-dimentional variational wind synthesis tool. The different datasets and the analysis technique employed will be discussed in Chapter 2. The evolution of Hurricane Ophelia throughout its lifetime, as well as the results from the rainband analyses and momentum budget analyses will be discussed in Chapter 3. Concluding remarks are offered in Chapter 4.

CHAPTER 2

DATA & METHODS

2.1 RAINEX & AIRBORNE RADAR DATA

The main dataset fundamental to this study is the airborne radar dataset from the Hurricane Rainband and Intensity Change Experiment (RAINEX) in 2005 (Houze et al. 2006). The goal of RAINEX was to utilize a high-resolution numerical weather model alongside aircraft observations to investigate the roles of eyewalls and rainbands in influencing TC intensity change. Throughout the duration of the RAINEX field campaign, three hurricanes were extensively observed: Katrina, Ophelia, and Rita. The study herein revolved around observations made in Hurricane Ophelia on 11 September 2005. Three aircraft were involved in RAINEX: two of NOAA's P-3 aircraft, referred to as N42 and N43, and the Naval Research Laboratory's (NRL) P-3 aircraft. Airborne radar data used in this study were from the N43 and NRL P-3 aircraft.

N43 was equipped with a single-parabolic antenna which alternately scans fore and aft to achieve dual-Doppler measurements (Jorgensen et al. 1996). This results in an along-track sampling resolution of approximately 1.5 km. The NRL P-3 was equipped with the National Center for Atmospheric Research (NCAR) dual-beam Electra Doppler Radar (ELDORA; Hildebrand et al. 1996), which has an along-track sampling resolution of about 0.4 km. One of the sampling strategies employed by RAINEX was to make "quad-Doppler" measurements of the rainbands. This involved two aircrafts flying on either side of the rainband and simultaneously sampling the wind components inside the rainband, thus producing the most reliable wind estimates (Jorgensen et al. 1996).

On 11 September, there were four periods during which N43 and NRL were simultaneously sampling Ophelia's rainbands - allowing for quad-Doppler wind retrievals. These four periods were separated into four different legs which are listed in Table 2.1, while the location of each of these four legs relative to the storm center is shown in Figure 2.1. Note that while these four legs mainly represent observations made in different sections of Ophelia's rainbands, they also represent a time evolution of the rainbands. To better represent this fact, these four legs will henceforth be referred to by the time the NRL aircraft began observations for that leg.

2.1.1 Radar Data Quality Control & N43 Reflectivity Correction

Both the N43 and NRL radar data were retrieved from Earth Observing Laboratory's webpage for RAINEX (EOL; www.eol.ucar.edu/field_projects/rainex). The N43 radar data was first corrected for

TABLE 2.1. The start and end of observation periods for the NRL and N43 aircraft.

Aircraft	Start Time (UTC)	End Time (UTC)
NRL	185301	190858
N43	185400	191037
NRL	201801	210558
N43	203002	210557
NRL	213341	215158
N43	212003	214257
NRL	215401	221059
N43	215403	220315

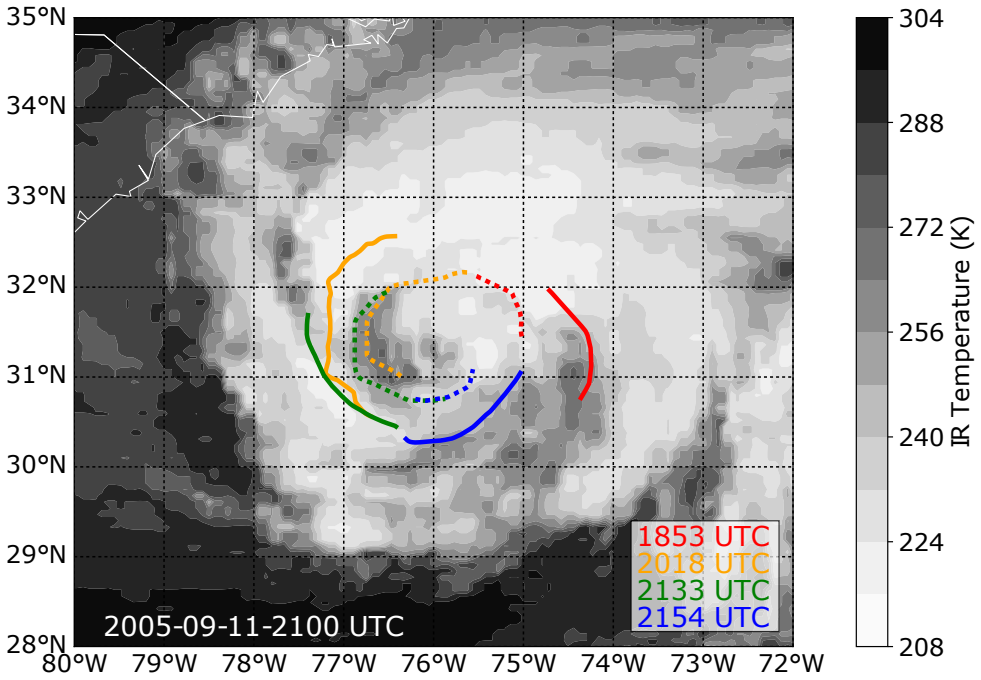

FIG. 2.1. The NRL (solid) and N43 (dashed) flight track along Ophelia's rainbands for the 1853 UTC Leg (red), 2018 UTC Leg (orange), 2133 UTC Leg (green), and 2154 UTC Leg (blue), overlaid on gridded IR image of Ophelia at 2100 UTC. Detailed observation times for both aircraft can be found in Table 2.1.

navigational errors (Testud et al. 1995), while the NRL radar data provided had already been corrected for navigational errors. The radar sweep files were then chosen according to the corresponding legs in Table 2.1. The radar images were initially quality controlled (QC) to remove any non-meteorological echo and instrument noise using the medium QC algorithm developed by Bell et al. (2013). The remaining non-meteorological echoes and noise were then manually removed. All of the foregoing QC steps were done using NCAR's Solo II software (Bell et al. 2013).

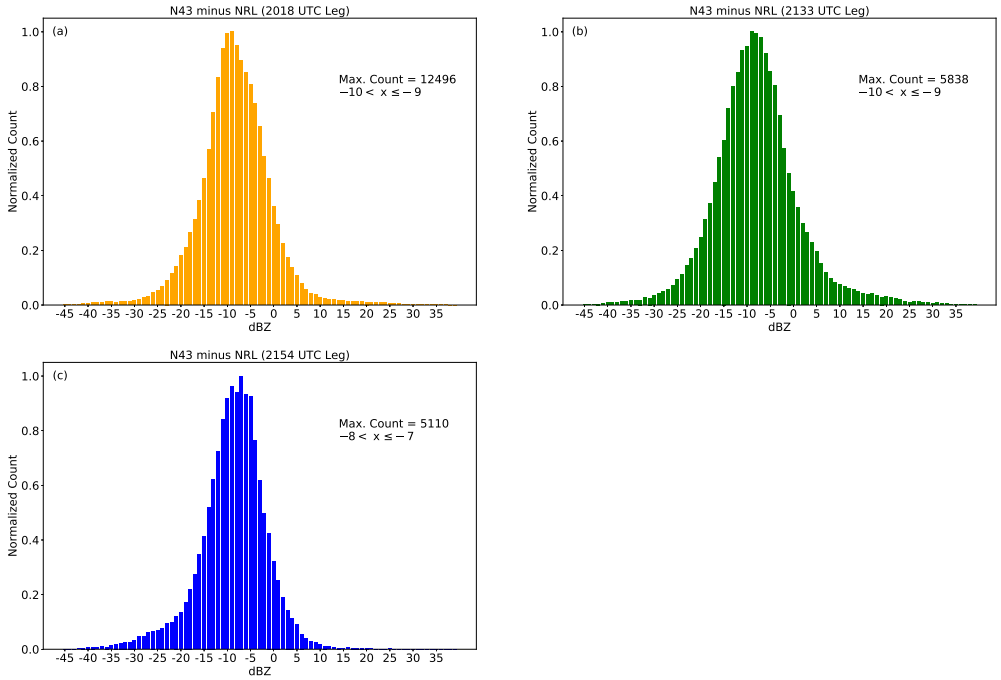

FIG. 2.2. Normalized distributions in the radar reflectivity (dBZ) difference between the N43 reflectivity field and the NRL reflectivity field (N43 minus NRL) for the (a) 2018 UTC Leg, (b) 2133 UTC Leg, and (c) 2154 UTC Leg.

The N43 radar reflectivity field was found to have a low bias relative to the NRL radar. To correct for this bias, the NRL radar was used as a "true" measurement with the assumption that it is well-calibrated. First, the reflectivity field from N43 and NRL from each flight leg was independently interpolated onto a Cartesian grid of the same resolution using SAMURAI. A brief description on SAMURAI will be offered in the following sections. For each data point containing both N43 and NRL reflectivity values, the NRL reflectivity value was subtracted from that of the N43. Subsequently, a histogram of the difference in reflectivity in each leg was plotted (Fig. 2.2). The resulting distributions were all Gaussian, centered at around -10 dBZ, indicating that the N43 radar had a negative bias relative to the NRL radar. There was a temporal lag between the N43 observations and NRL observations in the 1853 UTC Leg which resulted in a wider distribution in reflectivity difference between N43 and NRL (not shown). Therefore, data from the 1853 UTC Leg were excluded from subsequent calculations for the N43 reflectivity bias corrections.

Radar reflectivity (dBZ) is a logarithmic quantity, related to its linear form of radar reflectivity factor (z) by: $\mathrm{dBZ} = 10\log_{10} z$. Therefore, one cannot simply take an average of the dBZ distribution, as values of different orders of magnitudes in the linear scale may be calculated on the same order in the logarithmic scale. Typically, the reflectivity difference is converted into z, averaged, and then converted back to

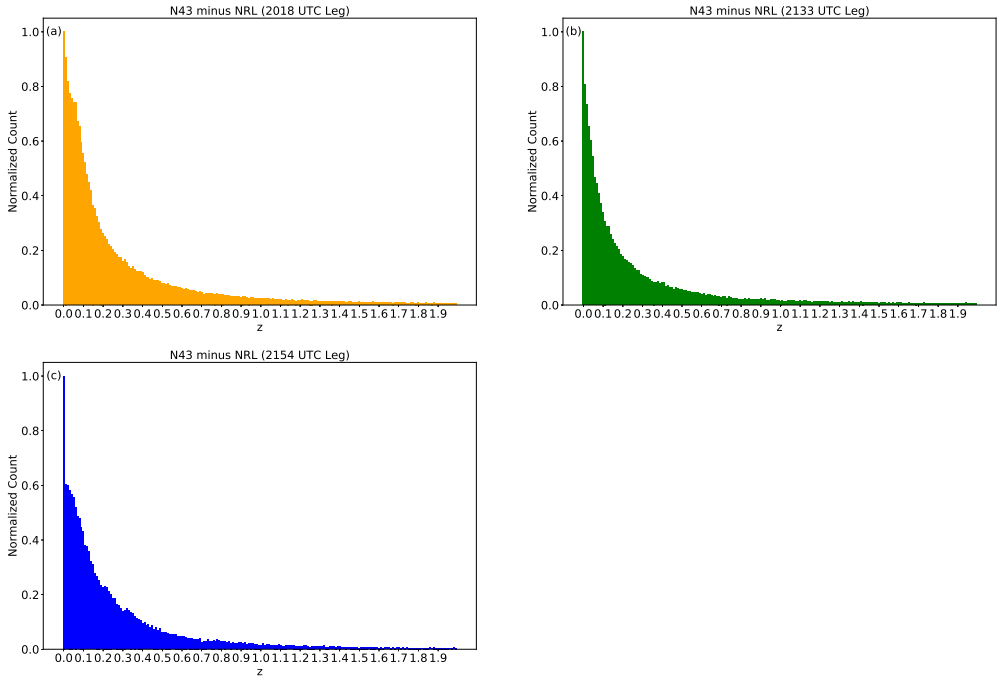

FIG. 2.3. Normalized distribution in the radar reflectivity factor (z) difference, calculated from the corresponding radar reflectivity distributions in Figure 2.2.

dBZ to obtain a single offset value. However, the corresponding z distributions were exponential with a long positive tail for all flight legs (Fig. 2.3). This likely resulted from the slight time lag between the observations from the two moving platforms, the time lag from moving convective elements, a product of the Cartesian interpolation, or a combination of all three factors. Thus, the extrema of the distribution in z dominated the averaging, which, when converted back to dBZ, produced a single dBZ offset value that is of the opposite sign to the distribution in Fig. 2.2. Therefore, the median of the distribution in z was used instead to obtain a single dBZ offset value for each leg. The single offset values from the 2018 UTC, 2133 UTC, and 2154 UTC Legs were then averaged, and the averaged single dBZ offset value of 7.87 dBZ was then added to the original N43 reflectivity (dBZ) field.

Fig. 2.4 shows the reflectivity field at 2 km altitude from NRL, and from N43 after and before the reflectivity correction was applied. Overall, the NRL reflectivity field (Fig. 2.4a) is better represented in the N43 bias-corrected reflectivity field (Fig. 2.4b), compared to before the bias correction was applied (Fig. 2.4c). The main purpose for doing the bias correction was to improve the application of the convective-stratiform partitioning algorithm (Didlake and Houze 2009). Since no quantitative precipitation estimations were made using the reflectivity field, the bias-corrected reflectivity field, though not perfect, was sufficient for the purpose of this study.

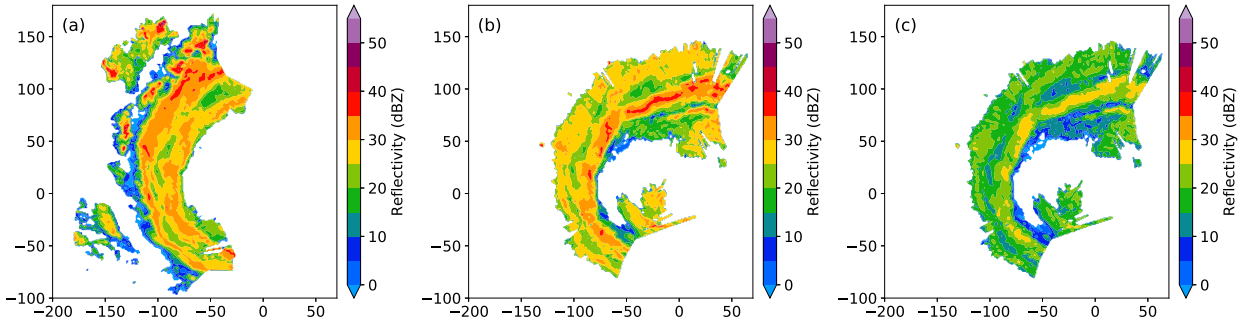

FIG. 2.4. (a) NRL radar reflectivity field, (b) corrected N43 radar reflectivity field, and (c) the uncorrected N43 radar reflectivity field at 2 km altitude from the 2018 UTC Leg.

2.1.2 Dual- vs Quad-Doppler Comparison

Quad-Doppler measurements require two separate observations to closely overlap in space and time. However, this was not necessarily the case for the dataset herein, particularly for the 1853 UTC Leg. During the 1853 UTC Leg, N43 was flying a north-to-south track, while NRL was flying in the opposite direction during the same ∼17-minute period. Moreover, the observations made by either aircraft overlapped one another for only a portion of their respective flights - which resulted in quad-Doppler measurements for only a portion of the flight leg and dual-Doppler measurements for the rest. Similar cases were observed in other flight legs. However, this should not affect the analysis and the conclusion made in this study. Fig. 2.5 shows the radius-height profile of the analyzed azimuthally-averaged tangential wind field (top panels) and radial wind field (bottom panels) for the 1853 UTC Leg. The left panels are analysis made from dual-Doppler wind retrievals from the NRL aircraft, the middle panels are analysis made from quad-Doppler wind retrievals, and the right panels are the difference between them (azimuthally-averaged NRL minus azimuthally-averaged quad-Doppler).

The largest difference in the radial and tangential wind field between a dual-Doppler and a quad-Doppler analysis was on the inner edge of the rainband (Fig. 2.5c,f). This was to be expected, since NRL was flying on the outer edge of the rainband while N43 was flying on the inner edge. Therefore, new information was added in the quad-Doppler analysis compared to the dual-Doppler analysis, particularly on the inner edge. The addition of the N43 radar data in the quad-Doppler analysis certainly improved the analysis. This was clearly seen in the unrealistically sharp gradient of tangential wind on the inner edge of the rainband in the dual-Doppler analysis (Fig. 2.5a) that was absent in the quad-Doppler analysis (Fig. 2.5b). However, elsewhere, the difference between the dual- and the quad-Doppler analysis was approximately ± 2 m s^{-1}, which is within the inherent margin of error associated with airborne

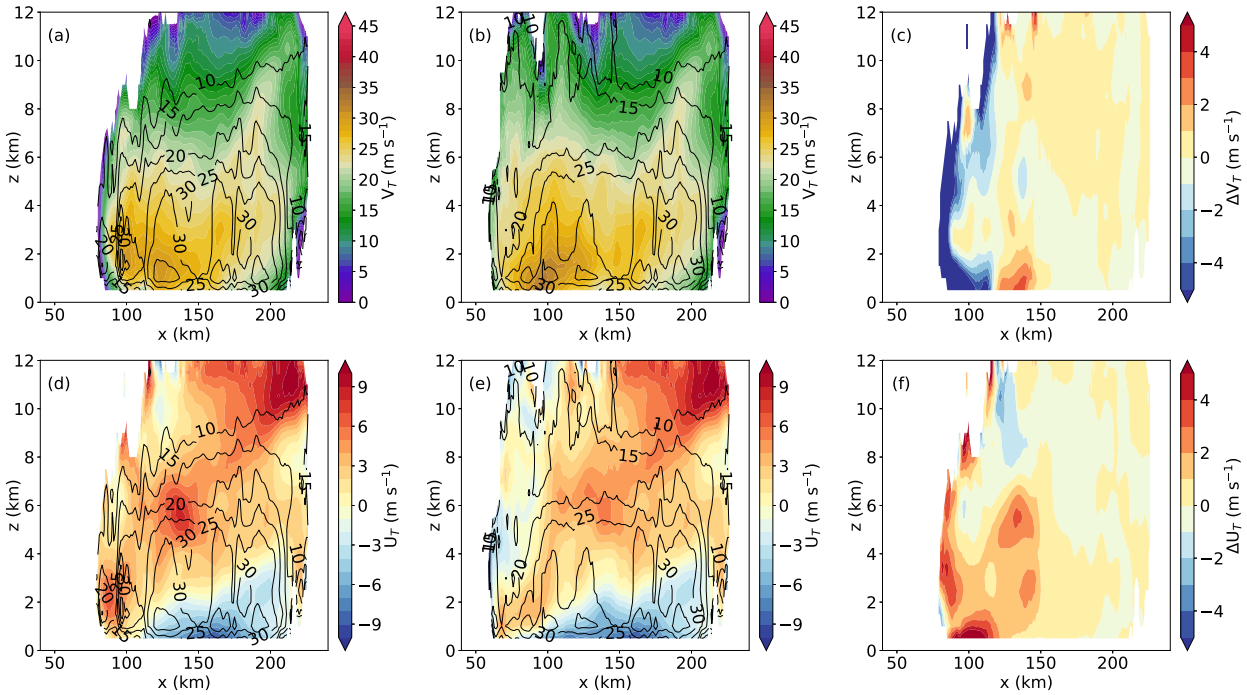

FIG. 2.5. Top: Azimuthally-averaged tangential winds (m s^{-1}) from (a) dual-Doppler analysis of the NRL radar data alone, (b) quad-Doppler analysis of both the NRL and the N43 radar data, and (c) the difference between (a) and (b) ((a) minus (b)). Bottom: Azimuthally-averaged radial winds (m s^{-1}) from (d) dual-Doppler analysis of the NRL radar data alone, (e) quad-Doppler analysis of both the NRL and the N43 radar data, and (f) the difference between (d) and (e) ((d) minus (e)). The analyses are of the 1853 UTC Leg.

Doppler synthesis (Hildebrand et al. 1996). In addition, the overall qualitative structure of the radial and tangential winds, which are the focus of this study, did not drastically change between the dual- and quad-Doppler analysis.

Since the differences between the dual- and quad-Doppler analysis in the other flight legs were less prominent than the examples shown here, and that the differences in the examples shown here did not drastically alter the analyzed wind field, the difference in the amount of quad-Doppler vs dual-Doppler measurements made during a flight leg should not affect the conclusion of this study. The analysis from the NRL radar alone is generally sufficient because of its high resolution and the addition of the N43 radar data only served to slightly improve the analysis.

2.2 BEST TRACK, SHIPS, GRIDSAT & OISST

Information on Hurricane Ophelia's track and intensity were obtained from the best track dataset (Jarvinen et al. 1984; McAdie et al. 2009; Landsea and Franklin 2013), while information on the environmental shear around Ophelia throughout its lifetime were obtained from the Statistical Hurricane

Intensity Prediction Scheme dataset (SHIPS; DeMaria et al. 2005). The environmental shear variables obtained for this study were the direction (degree heading) and magnitude (m s^{-1}) of the 850 to 200 hPa shear over an annulus of 200 to 800 km from the center of the storm (SHTD and SHRD), and of the 850 to 200 hPa shear over an annulus of 0 to 500 km from the 850 hPa vortex center (SDDC and SHDC). Both the best track dataset and the SHIPS dataset were obtained from The Enhanced Vortex Data Message Dataset (VDM+) compiled by Vigh (2015).

To provide a reference image of the storm-relative flight track (Fig. 2.1) for the observation period that began at 1853 UTC and ended at 2210 UTC on 11 September 2005, a gridded satellite infrared image of Hurricane Ophelia at 2100 UTC was used (GRIDSAT-B1; www.ncdc.noaa.gov/gridsat). Meanwhile, the evolution of the daily sea surface temperature (SST) around Hurricane Ophelia from the 9^{th} to the 14^{th} was illustrated using the Daily Optimum Interpolation Sea Surface Temperature (OISST) dataset from the National Oceanic and Atmospheric Administration (NOAA) National Centers for Environmental Information (NCEI; www.ncdc.noaa.gov/oisst). The OISST blends observations from satellites, ships, and buoys to provide a spatially complete SST map at 0.25 degree spatial resolution (Banzon et al. 2014).

2.3 Flight-Level Dataset & Satellite Microwave Imagery

The evolution of Ophelia's tangential wind field was analyzed using flight-level data from the United States Air Force (USAF) aircraft reconnaissance missions. The flight level data were obtained from FLIGHT+: The Extended Flight Level Dataset for Tropical Cyclones (Version 1.1; Vigh et al. 2016). In a typical hurricane aircraft reconnaissance mission, the aircraft would fly multiple radial paths that transect the center of the TC, providing radial profiles of flight-level dynamic and thermodynamic variables in different quadrants of the storm. Each flight track towards or away from the center of the TC is considered as one radial leg. The USAF C-130 aircraft flew at the 700 mb level in nine reconnaissance flights into Hurricane Ophelia, with a minimum number of six radial legs in each mission. For each mission, the radial profile of the tangential wind was azimuthally averaged, before being smoothed using a 10-km low-pass Lanczos filter.

Integrated kinetic energy (IKE) was calculated for each flight reconnaissance mission using the formula:

$$\text{IKE} = \int_{r_1}^{r_2} \rho \, \frac{U_T^2 + V_T^2}{2} \, dr$$

Where ρ is the flight-level air density and was calculated from the flight-level thermodynamic variables through the ideal gas equation $\rho = \frac{P}{R\,T}$, where $P = 700\,\text{hPa}$, T is the calculated flight-level virtual temperature, and R is the dry gas constant, $R = 287\,\text{J}\,\text{K}^{-1}\,\text{kg}^{-1}$. U_T and V_T are the respective flight-level radial and tangential winds. Similar to the flight-level tangential winds, the flight-level radial winds were also azimuthally averaged and smoothed using a 10 km low-pass Lanczos filter. Here, the values $r_1 = 5.8\,\text{km}$ and $r_2 = 170\,\text{km}$ were chosen to ensure consistency in the number of data points across all flight legs. The unit for IKE as calculated above is Joules per unit depth.

To complement the flight-level dataset, microwave imagery of Hurricane Ophelia were obtained from the Naval Research Laboratory Monterey Tropical Cyclones website (www.nrlmry.navy.mil/TC.html). The microwave sensors from which these images were retrieved are aboard polar-orbiting satellites which provide only a snapshot of the storm at a particular time. When available, the imagery closest to the time of each aircraft reconnaissance mission were selected, providing a corresponding satellite image for six of the nine aircraft reconnaissance missions. Satellite microwave imagery around the time the research flights were conducted were also retrieved, providing one image around the start of the research flight and two images after the conclusion of the research flights.

The images are of the 85-, 89-, 91-, and 37-GHz channel from Defense Meteorological Satellite Program's (DMSP) F-12, F-13, F-14 and F-16 satellites, the Tropical Rainfall Measuring Mission (TRMM) satellite, and NASA's Aqua-1 satellite. In the 85- to 91-GHz channels, large ice particles associated with deep convection scatters outgoing terrestrial radiation, resulting in low/cold brightness temperatures as observed from an earth-orbiting satellite. Thus, low/cold brightness temperatures in the 85- to 91-GHz channels serve as a proxy for the location of deep convection, providing an estimation on the distribution of convection in the storm associated with the corresponding observed flight-level tangential wind profile. The 37-GHz channel is sensitive to radiation emitted by liquid water in clouds, whether that be in the form of liquid cloud droplets or rain. Therefore, in the 37-GHz channel, low-level "warm clouds" and rain would appear as warm brightness temperatures compared to the ocean surface. The radiation detected in this channel is insensitive to scattering by ice particles above them. Thus, an image of the low-level cloud and precipitation fields associated with shallow convection could be retrieved, even if they occurred underneath the TC cirrus shield.

2.4 Analysis

Quad-Doppler analysis of each leg was done using a spline-based three-dimensional variational wind synthesis tool known as SAMURAI (Bell et al. 2012). The analysis domain was centered at the center of the storm. Ophelia had moved very little on the day the observations were made. Therefore, the storm motion was assumed to be stationary, with the storm centered at 31.39°N 75.94°W. The storm center used for the analysis is based on the Best Track data at 1800 UTC on the 11^{th}, and was manually adjusted to best fit the observed reflectivity field. The analysis was initially done on a Cartesian plane, with a horizontal resolution of 1 km and a vertical resolution of 0.5 km. The analysis fields were then interpolated onto cylindrical coordinates with 1 degree azimuthal resolution and 1 km radial resolution, to allow for interpretation of the storm variables along the arc of the rainbands.

CHAPTER 3

RESULTS

3.1 HURRICANE OPHELIA (2005)

Ophelia (2005) began as a remnant cold front that moved off the eastern coast of the United States on September 1st. The front merged with an elongated trough that stretched from Tropical Depression Lee east of Bermuda to near the Florida Peninsula. An area of low pressure that would soon become Ophelia formed near the Bahamas on September 4th and drifted southward. On September 5th, precipitation associated with the area of disturbance became better organized and the disturbance began moving northward. Around 0600 UTC 6 September, the disturbance was classified as a tropical depression. The best track center position and intensity of the tropical cyclone are shown in Fig. 3.1 and Fig. 3.2 respectively. Information on the environmental shear throughout the storm's life cycle is shown in Fig. 3.3. The tropical depression proceeded on a northward track, becoming a tropical storm around 0600 UTC 7 September.

Tropical Storm Ophelia intensified steadily as it made a counter-clockwise loop off the Florida east coast between 1800 UTC 7 September and 0000 UTC 9 September, where it briefly became a Category 1 hurricane. It was downgraded back to a tropical storm by 0600 UTC 9 September. By 1800 UTC 9 September, Ophelia became a Category 1 hurricane again as it moved out into the open ocean and away from land, only to be downgraded to a tropical storm again six hours later. As Ophelia became a Category 1 hurricane for the third time in its lifetime at 1200 UTC 10 September, it was about to make a slow clockwise loop. Between 1800 UTC 10 September and 1800 UTC 11 September, the storm was relatively stationary. At this point, Hurricane Ophelia was located over cold ocean water that was upwelled due to its own wind field. Note that the daily average sea surface temperature (SST) over which Ophelia was located was as cold as 23.5°C (Fig. 3.4c), significantly below the theoretical threshold of approximately 26.5°C needed for TC genesis and sustenance (Dare and McBride 2011).

By 0000 UTC 12 September, Ophelia was a tropical storm again. It remained so as it continued moving up along the east coast of the United States, becoming a Category 1 hurricane for a fourth time at 0000 UTC 14 September. Ophelia reached its peak intensity of 75 knots for the second time at 1200 UTC 14 September, not long before it made its closest approach to land. However, hurricane-force winds remained offshore. By 0000 UTC 16 September, it weakened into a tropical storm for the last time as it accelerated northeastward, underwent extratropical transition at 0000 UTC 18 September,

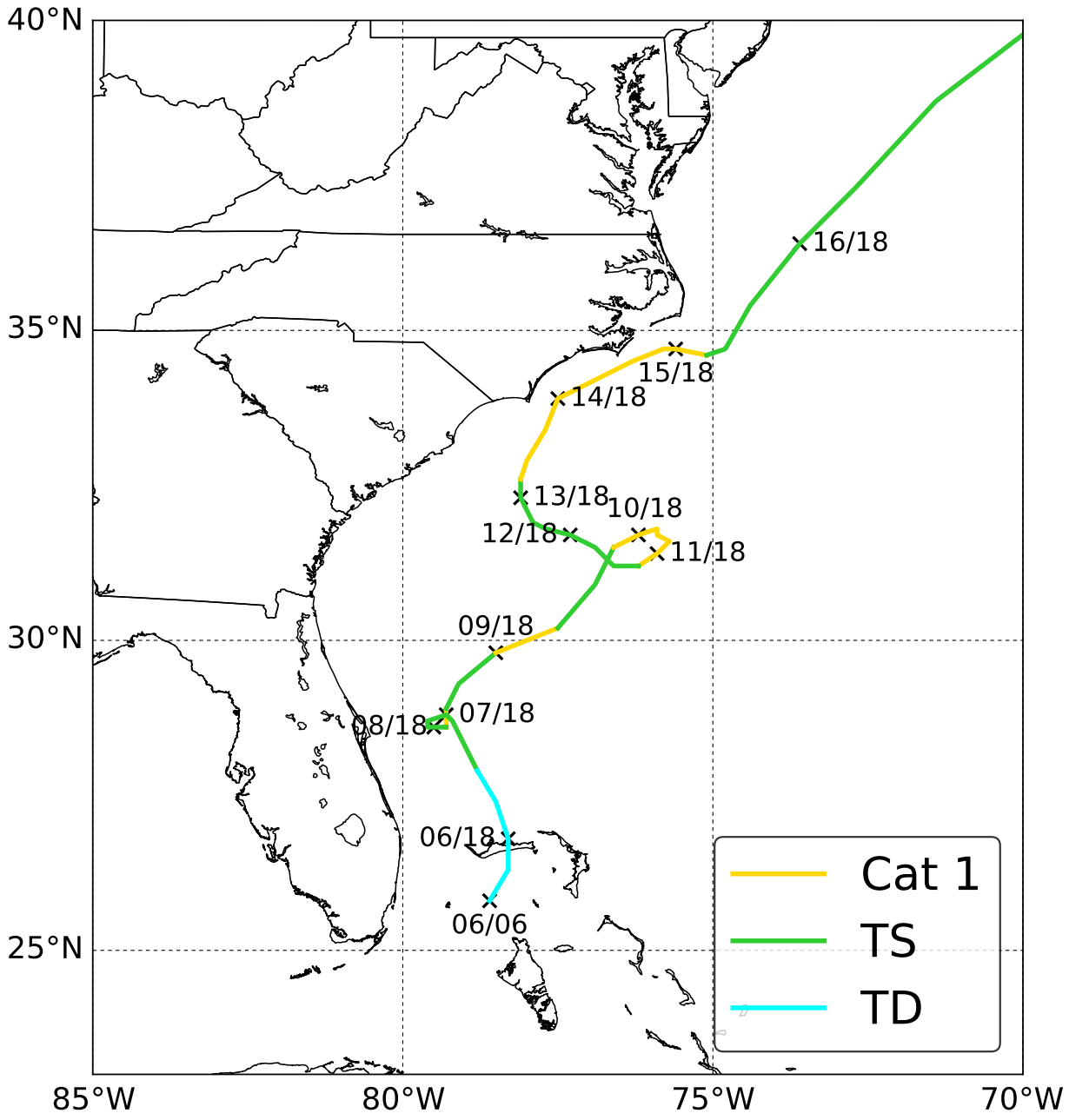

FIG. 3.1. Ophelia's track and intensity from the National Hurricane Center's best track dataset. The intensity classifications are tropical depression (TD; turquoise), tropical storm (TS; green), and Category 1 Hurricane (Cat 1; yellow). A select few best track center locations and the corresponding dates and times in UTC are labeled along the storm track.

and dissipated by 0600 UTC 23 September. A more detailed discussion on Hurricane Ophelia throughout its lifetime can be obtained from the National Hurricane Center's Tropical Cyclone report (NHC; www.nhc.noaa.gov/data/tcr/).

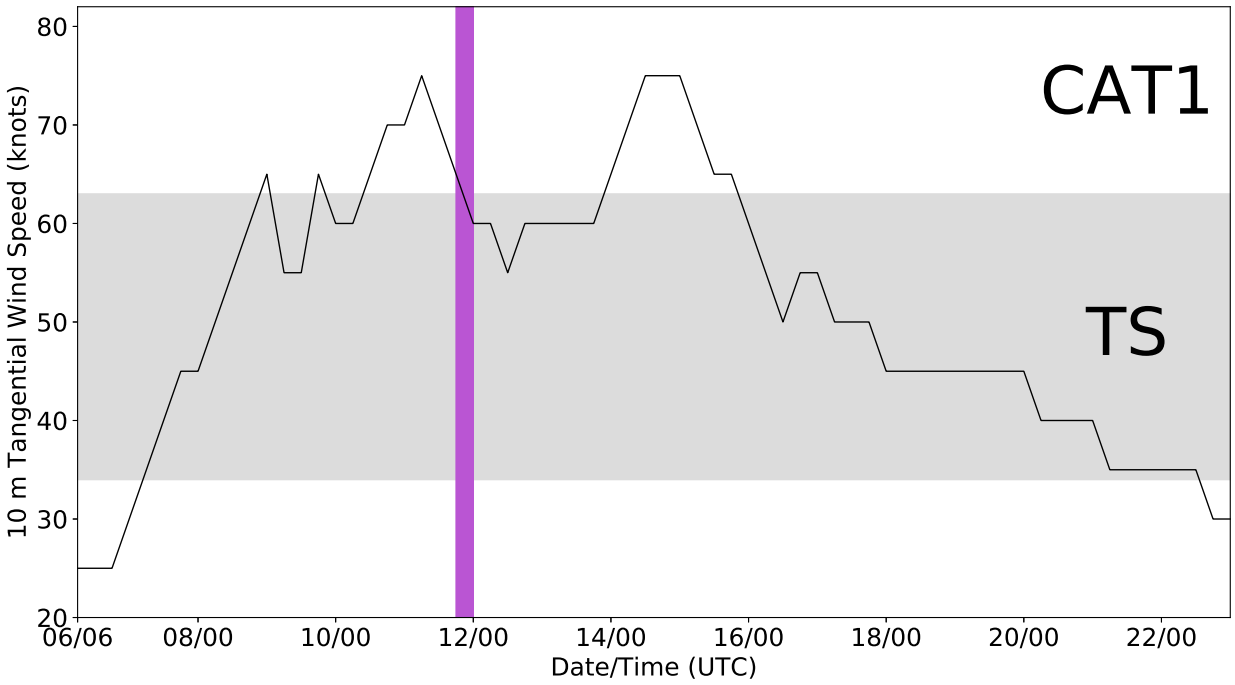

FIG. 3.2. The evolution of Ophelia's intensity (defined by the maximum 1-minute sustained wind at 10 meters, in knots) from the National Hurricane Center's best track dataset. The purple line indicates the approximate time when observations were made on September 11th. The labels indicate tropical storm (TS) and Category 1 (CAT1) intensity.

3.2 FLIGHT-LEVEL TANGENTIAL WIND EVOLUTION

The evolution of Ophelia's tangential wind field as observed by nine aircraft reconnaissance missions is shown in Fig. 3.5. The corresponding satellite microwave imagery for six out of the nine aircraft reconnaissance missions are shown in Fig. 3.6. The flight-level tangential winds at 1130 UTC 10 September were characterized by a single peak of about 34 m s^{-1} (primary wind maximum), with a radius of maximum wind (RMW) at about 50 km. At this point, Ophelia was a weak Category 1 hurricane on its way to becoming a strong Category 1 hurricane for the first time (Fig. 3.2). Based on satellite microwave imagery at this time, Ophelia's eyewall was only distinguished by convection located on the northern periphery of the eye (Fig. 3.6a), at about the same distance as the RMW. Immediately outside and almost connected to the eyewall, convection associated with an inner rainband was seen spiraling outward from the northeast to the southwest. There was no indication of a secondary wind maximum at flight level associated with the rainband convection. However, this does not rule out the existence of a secondary wind maximum at other vertical levels. Farther out, more convection was seen in Ophelia's northeast quadrant, probably associated with an outer rainband.

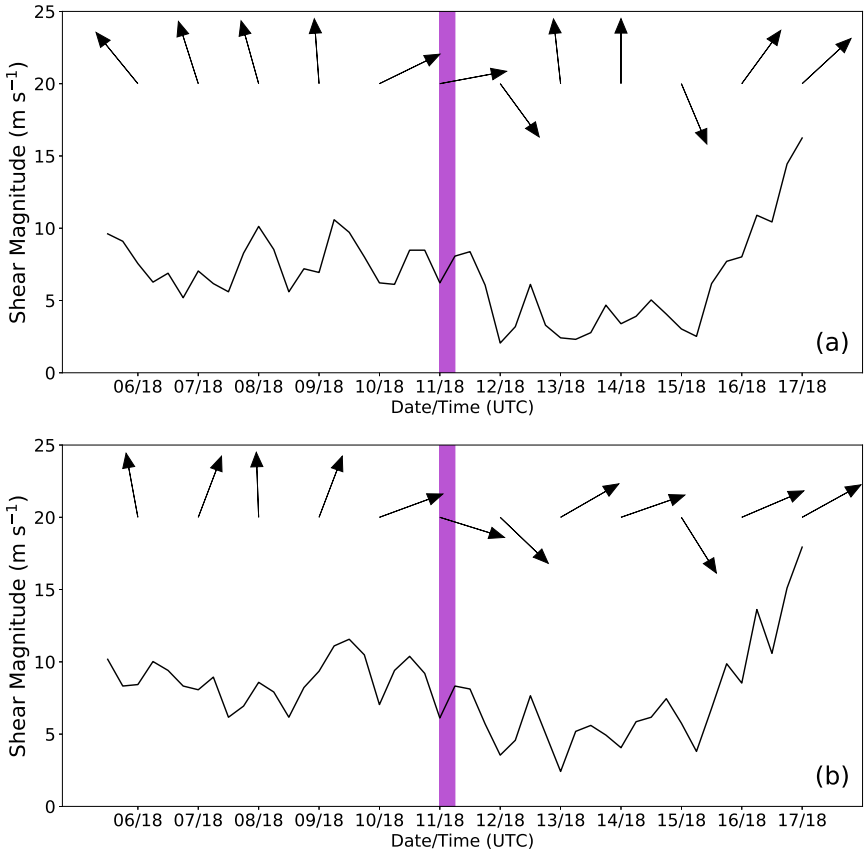

FIG. 3.3. Direction (degree heading) and magnitude (in m s^{-1}) of the 850-200 hPa environmental shear around Ophelia throughout its life cycle from the Statistical Hurricane Intensity and Prediction Scheme (SHIPS) dataset. A 90° heading means that the shear vector is pointed east. (a) Shear magnitude and heading averaged from 0-500 km radius around the center of the 850 hPa vortex (SHDC and SDDC). (b) Shear magnitude and heading averaged from 200-800 km around the center of the storm (SHRD and SHTD). The purple line indicates the approximate time when observations were made on September 11th.

By 2245 UTC 10 September, Ophelia's tangential wind had strengthened slightly while its RMW had also contracted slightly. The northern portion of Ophelia's eyewall remained convectively active at around the RMW, while the southern portion of the eyewall appeared "broken" with no apparent deep convection (Fig. 3.6b). In addition, the convection in the inner rainband had weakened significantly. At 0030 UTC 12 September, Ophelia's primary wind maximum had weakened, and there was a secondary wind maximum of about 31 m s^{-1} at a radius of 95 km from the center of the storm. Satellite microwave imagery showed convection in Ophelia's eyewall had dissipated (Fig. 3.6c). Instead, there were two bands of convection associated with one or possibly more rainbands. The inner band of convection spiraled outward from the north to the east at approximately the radius of the secondary wind

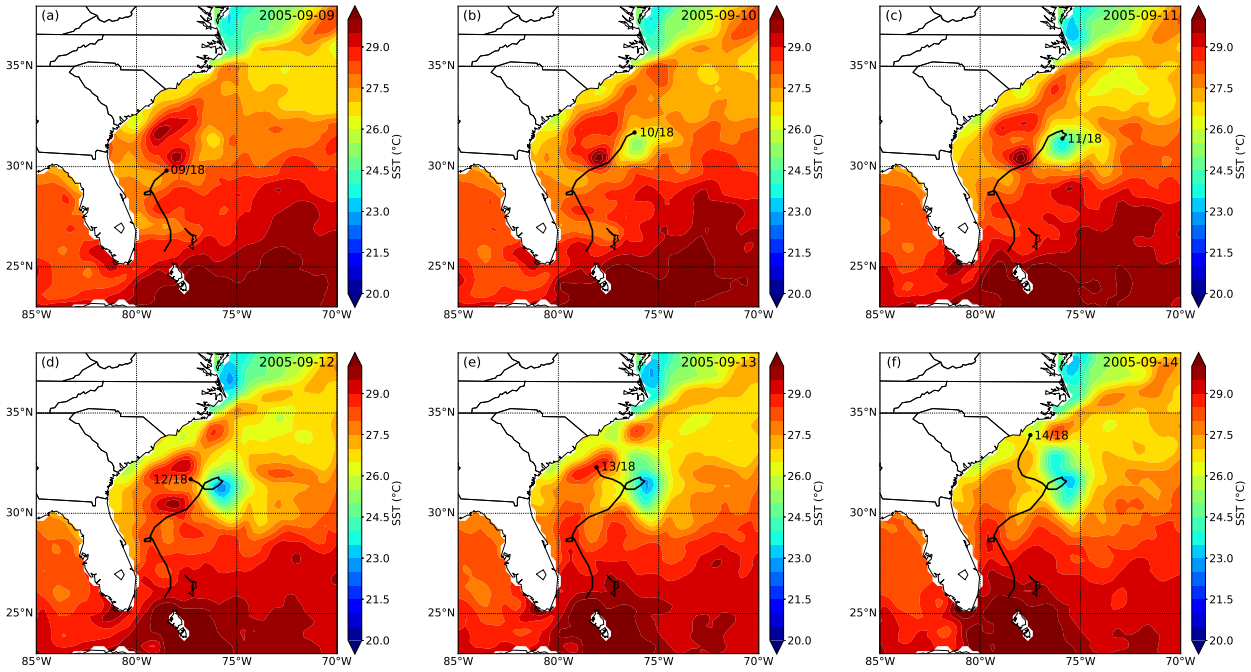

FIG. 3.4. Daily average sea surface temperature (SST; °C) overlaid with Ophelia's track up until 1800 UTC of the corresponding day. The dates are labeled in the top right corner of each figure.

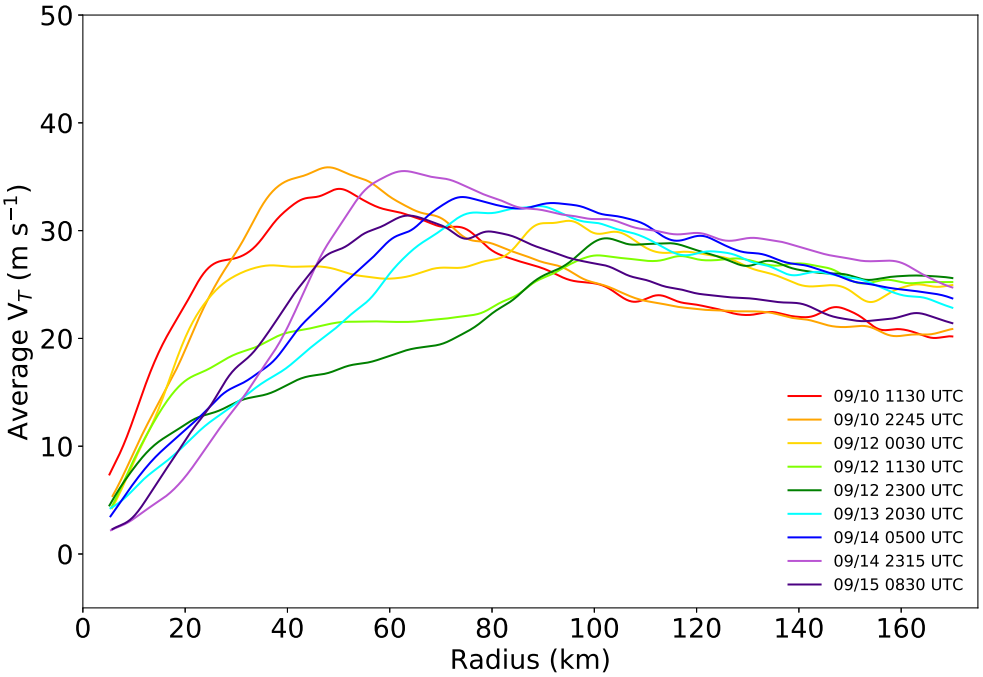

FIG. 3.5. The evolution of Ophelia's flight-level (700 hPa) tangential wind field as observed from nine US Air Force aircraft reconnaissance missions. The start time of the first radial pass during each reconnaissance mission is labeled.

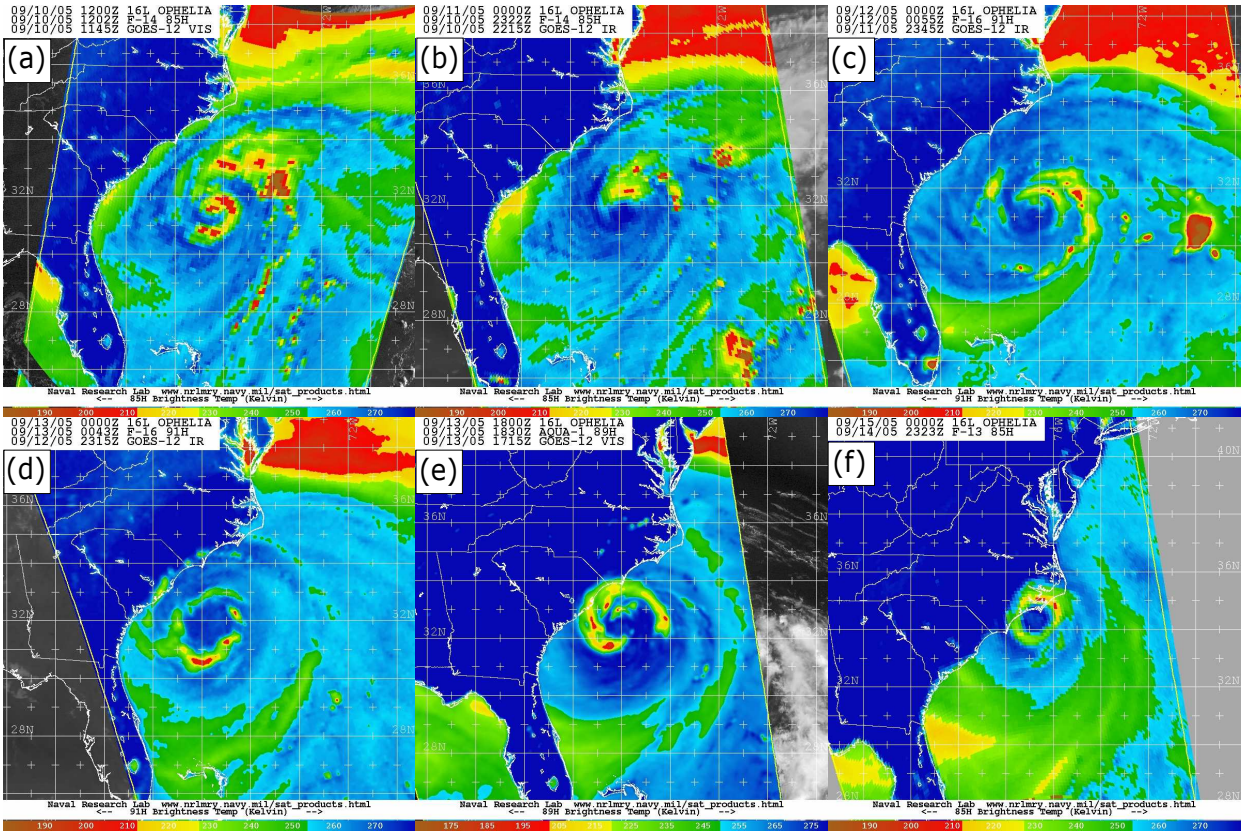

FIG. 3.6. Satellite microwave imagery of Hurricane Ophelia as it underwent an eyewall replacement cycle.

maximum, while the outer band of convection spiraled outward from the northeast to the south. At this time, Ophelia had just weakened back into a tropical storm.

At 2300 UTC 12 September, the primary wind maximum had completely dissipated. The secondary wind maximum at a radius of 102 km had become the primary wind maximum. Concurrently, Ophelia's eye had gotten larger as it was surrounded by a near-circular band of convection, with stronger convection to the south and weaker convection to the north (Fig. 3.6d). At this time, Ophelia's intensity was at a relative minimum (Fig. 3.2). As Ophelia was re-intensifying at 2030 UTC 13 September, the RMW had contracted to a radius of 89 km. At this time, the storm had begun tracking away from colder SSTs over into warmer SSTs (Fig. 3.4c,d). Associated with the warmer SSTs, there was some indication that eyewall convection was beginning to be re-invigorated, with a region of convection seen on the northern periphery of the eye (Fig. 3.6e). Ophelia's rainband also appeared to have assumed its original spiral structure. By 2315 UTC 14 September, Ophelia's RMW had contracted to a radius of 63 km, with eyewall convection surrounding the eye at approximately the same radius.

The foregoing discussion on the evolution of Ophelia's tangential wind field alongside changes in the distribution of eyewall and rainband convection bears strong resemblance to an eyewall replacement cycle (ERC). Based on the schematic of ERC progression by Sitkowski et al. (2011) and the flight-level tangential winds, Ophelia's intensification and weakening phases must have occurred long before 0030 UTC 12 September, and its re-intensification phase occurred around 0030 UTC 12 September. While ERCs are fairly common in major TCs (Category 3 or above on the Saffir-Simpson Hurricane Wind Scale), ERCs in a Category 1 TC such as Ophelia are rare. Nevertheless, a common feature typically associated with all ERCs is the broadening of the tangential wind field. Such a feature was indeed observed in Ophelia. The RMW and stronger winds were observed at larger radii after the emergence of the secondary horizontal wind maximum at 0030 UTC 12 September. An important implication to the broadening of the tangential wind field associated with an ERC is that tropical-storm-force or hurricane-force winds can occur at larger radii, creating a larger damage swath.

The broadening of the tangential wind field was clearly evident when viewed in the context of integrated kinetic energy per unit depth (IKE; Fig. 3.7). The broadening of the tangential wind field is pronounced when viewed in the terms of IKE because IKE is influenced by a radius factor, whereby strong winds at larger radii would result in a larger IKE compared to equally strong winds at smaller radii. The explanation for the evolution of the IKE is as follows. At 1130 UTC and 2245 UTC 10 September, the tangential wind field was nearly identical. The RMW was at around 50 km at both times, with the primary wind maximum at 2245 UTC being slightly stronger. The resulting IKE at 2245 UTC was only slightly larger than that at 1130 UTC. The IKE increased to about 4.4 $\times 10^6$ J at 0030 UTC 12 September because of the presence of a secondary horizontal wind maximum at 95 km radius and the presence of stronger winds at larger radii. For example, the tangential wind speed at 100 km radius on 10 September was at around 25 m s^{-1}, whereas the tangential wind speed at 0030 UTC 12 September at the same radius was stronger at around 30 m s^{-1} (Fig. 3.5). The IKE at 0030 UTC 12 September was not significantly larger than the previous two times because the primary wind maximum was weaker than the previous two times.

Ophelia's IKE decreased to about 3.8 $\times 10^6$ J by 2300 UTC 12 September, mainly due to the dissipation of the old primary wind maximum and a weaker new primary wind maximum. As the new primary wind maximum strengthened and the RMW contracted, IKE increased to over 5.2 $\times 10^6$ J by 2315 UTC 14 September. The maximum in IKE is due to the combined effect of stronger winds at larger radii and

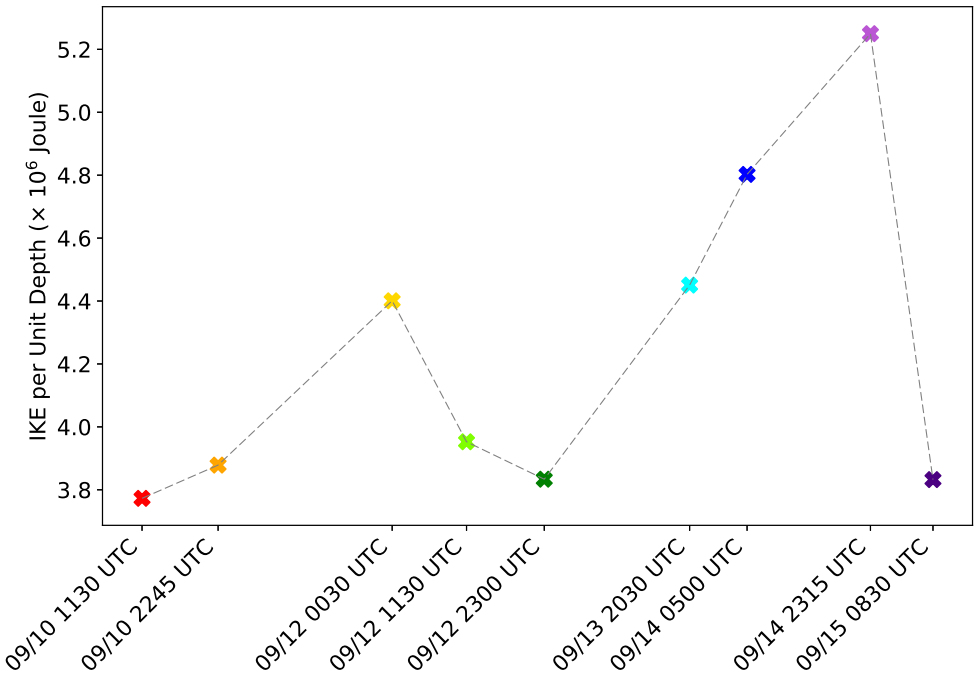

FIG. 3.7. The integrated kinetic energy (IKE) per unit depth calculated from the flight-level tangential wind profiles in Figure 3.5. The tick colors correspond to the times listed in Figure 3.5.

a larger RMW, even though the strength of the primary wind maximum at its peak is almost identical to the strength of the old primary wind maximum prior to the onset of the ERC (Fig. 3.5). By 0830 UTC 15 September, the IKE decreased again as Ophelia underwent further weakening before the storm transitioned into an extratropical system and dissipated.

3.3 RAINBAND ANALYSIS

The ERC observed in Ophelia presented an interesting case because it occurred when the storm was a Category 1 hurricane located over cold SSTs. Fortunately, RAINEX observations were made near the end of the weakening phase of the ERC - between approximately 1853 UTC and 2210 UTC on September 11th (purple line, Fig. 3.2). Quad-Doppler observations made in Hurricane Ophelia's rainband during that period offered clues on the roles of convective and stratiform precipitation in the observed ERC. Discussions on the observed rainband structure in the individual legs are presented below. The reference shear vector utilized for the following discussions were taken from the 0-500 km shear (SHDC and SDDC) at 1800 UTC 11 September, instead of the shear vector from the 200-800 km shear (SHRD and SHTD) (Fig. 3.3). The selection of the former shear vector was made because the distribution of convective and stratiform precipitation in Ophelia's rainbands relative to the chosen shear parameter during

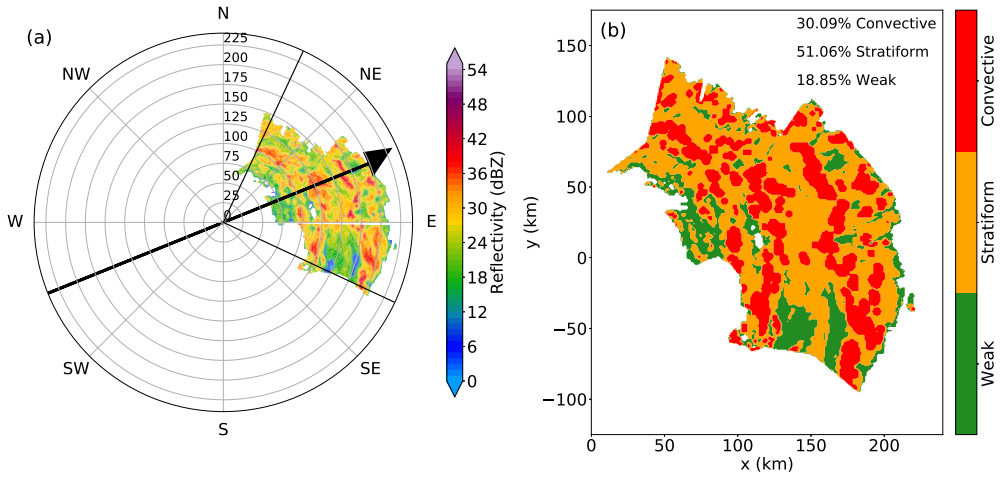

FIG. 3.8. (a) Radar reflectivity field at 2 km altitude with an overlaid arrow indicating the shear heading for the 1853 UTC Leg. The azimuthal angles from which the azimuthally-averaged cross-section was derived are indicated by the two black lines. (b) The corresponding result of the convective-stratiform algorithm.

the period of observation corresponded well with what is understood from previous literature (Hence and Houze 2012). The shear used for the following discussion had a heading of 79° (east-northeast) and a magnitude of 6.2 m s^{-1}.

3.3.1 1853 UTC Leg

The 1853 UTC Leg was located in the downshear quadrants of the storm, with a slightly bigger portion being in the right-of-shear quadrant (Fig. 3.8a). Based on the convective-stratiform partitioning algorithm, the 1853 UTC Leg was the most convectively active rainband out of the four legs observed in this study, with 30.09% of the radar echoes in this leg classified as convective (Fig. 3.8b). This corresponds well with previous studies that showed convection in TC rainbands being the most vigorous in the right-of-shear quadrants. Heavier precipitation can also be found in the downshear quadrants (Hence and Houze 2012). Convection in this leg was loosely organized into two bands that spiral in along with the rainband. This double-band convection feature was also observed in a RAINEX flight into the rainband of Hurricane Rita (Didlake and Houze 2013a).

To investigate the kinematic structure of the rainband in the 1853 UTC Leg, azimuthal averages of radial, tangential and vertical winds as well as reflectivity were taken between the two black lines in Fig. 3.8a. The azimuthal averages are shown in Fig. 3.9. These azimuthal averages preclude detailed analysis of the mesoscale structure of rainband convection. Rather, they represent the collective effect of convection throughout this leg. The 1853 UTC Leg was generally populated by shallow convection, with the 20 dBZ average reflectivity contour reaching up to an altitude of only 6 km. A closer

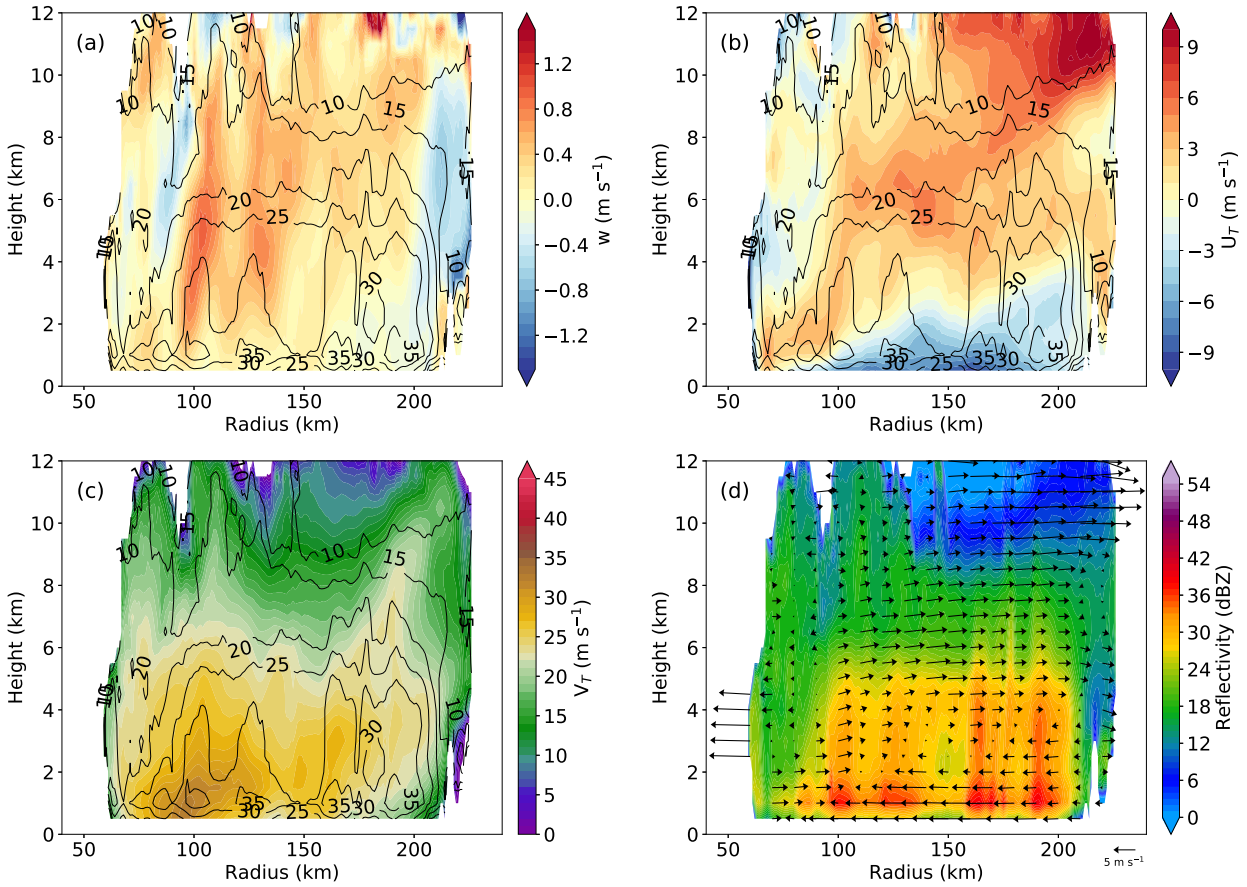

FIG. 3.9. Azimuthally-averaged (a) vertical, (b) radial and (c) tangential velocities (m s^{-1}) with overlaid contours of azimuthally-averaged reflectivity (dBZ), and (d) the azimuthally-averaged reflectivity (dBZ) with overlaid wind vectors in the 1853 UTC Leg.

inspection revealed two distinct regions of convection: the "inner" region between 70 - 150 km radius, and the "outer" region between 150 - 200 km radius. Each region was marked by two columns of local reflectivity maximum that are made apparent by the 30 dBZ reflectivity contour.

The inner region was dominated by shallower reflectivity columns that reached an average altitude of about 4 km, whereas the outer region was dominated by deeper reflectivity columns that reached an average altitude of 5 km. The collocation of a local low-level convergence maximum and upper-level divergence maximum with these reflectivity columns indicate that they are produced from convective updrafts (not shown). The spikes in the 20 dBZ contours in the outer region indicate the presence of deeper convection within the rainband that penetrate above the overlying TC cirrus shield associated with the eyewall outflow. A statistical analysis of the heights of these convectively-produced reflectivity columns (henceforth, convective columns for brevity), as well as the kinematics associated with them along the arc of the rainband will be presented later.

The shallow rainband convection and decreasing convective heights with radius has been well documented (Hence and Houze 2012; Didlake and Houze 2013a). This configuration of rainband convection has been attributed to the vertical shear of the horizontal winds produced by eyewall outflow that acts to limit the vertical extent of convection. Thus, the effect of the eyewall outflow increases with decreasing distance from the eye of the storm. The deeper convection observed in the outer region of the 1853 UTC Leg signified the eyewall outflow's weakening influence in limiting the vertical extent of rainband convection. The radius of approximately 200 km at which this weaker influence was observed closely matches the radius at which Hence and Houze (2012) hypothesized TC vortex dynamics having negligible effect on rainbands.

The 1853 UTC Leg was also characterized by a low-level inflow and an upper-level outflow, typical of a secondary circulation seen in convectively-dominant rainbands (Didlake and Houze 2013a). Similar to the observations made by Didlake and Houze (2013a), the depth of the radial inflow decreased with radius, with the inflow layer reaching up to an altitude of 4 km in the outer region and 2 km in the inner region (Fig. 3.9b). An updraft and an outflow maximum was seen above each convective column in the inner region, with the outflow layer decreasing in height radially inside the inner region. The updraft and outflow in the outer region were less apparent in this azimuthally-averaged view (Fig. 3.9a,b). There was a tangential wind maximum in the inner convective column of the inner region, just above the inflow layer at 1.5 km altitude (Fig. 3.9c). This tangential jet appears disorganized, occupied only a small portion of the leg, and dissipated by 4 km altitude. There was no significant tangential wind maximum associated with the convective columns in the outer region.

To understand the variation in the characteristics of convection along the arc of the rainband, contoured frequency by altitude diagrams (CFAD; Yuter and Houze 1995) were constructed. CFADs show the relative frequency distribution - along the arc of the rainband in this particular case - of a variable separated by height and normalized by the maximum in the distribution. CFADs of reflectivity, radial velocity, and tangential velocity were constructed for the inner and outer region (Fig. 3.10). The inner and outer regions were defined based on the radial extent of the convective columns in the azimuthal mean view (Fig. 3.9), with the location of the inner region defined as between 50 km and 150 km radius, and the location of the outer region defined as between 150 km and 210 km radius. The 50% frequency value is marked by the black contour overlaid on the CFAD filled contours, where the modal distribution is defined as the frequency above 50% of the distribution (Hence and Houze 2012).

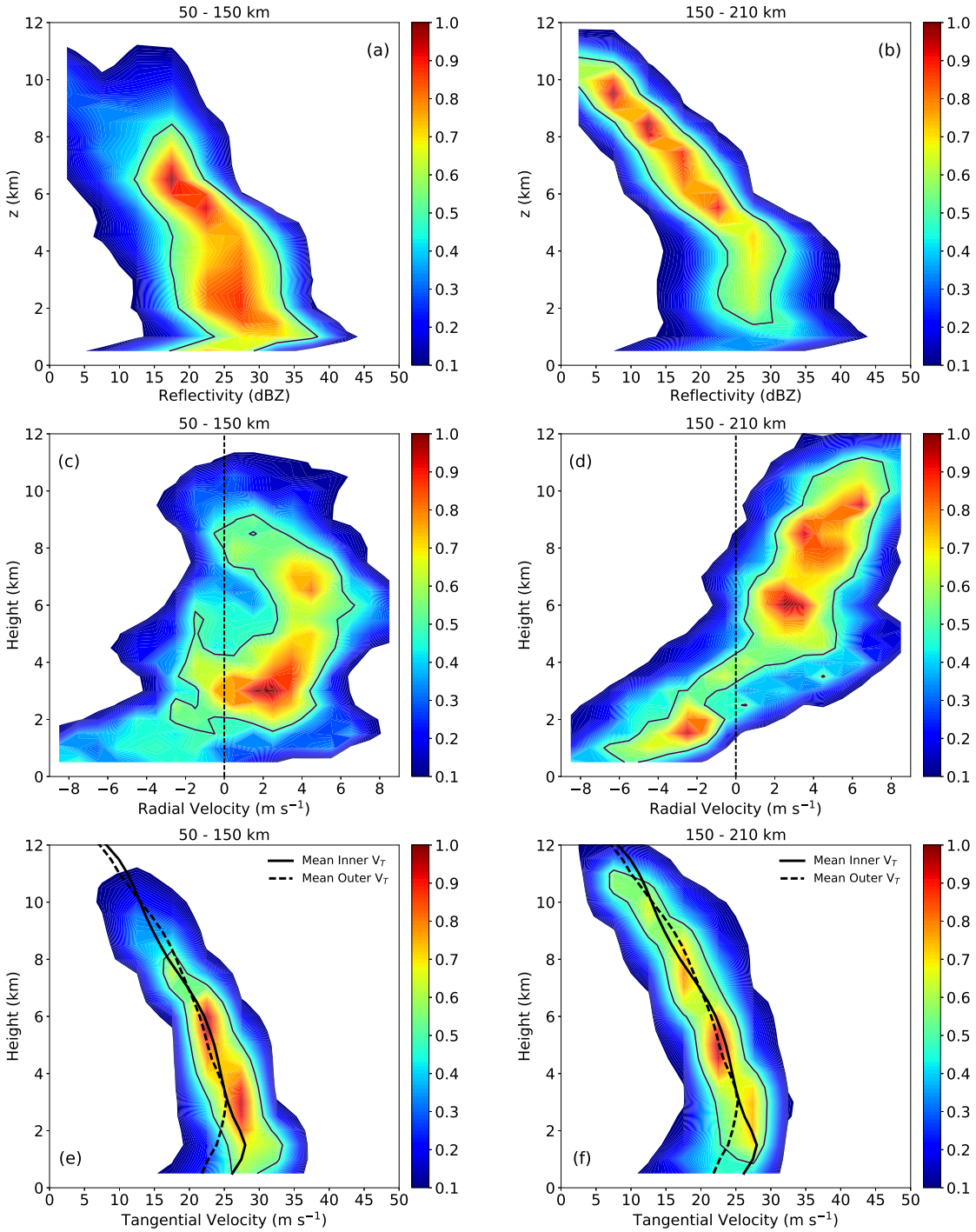

FIG. 3.10. Contoured frequency by altitude diagrams (CFADs) of reflectivity (dBZ; a,b), radial velocity (m s^{-1}; c,d), and tangential velocity (m s^{-1}; e,f) for the inner region (left column, 50 - 150 km radius) and outer region (right column, 150 - 210 km radius). A contour representing 50% frequency of the distribution was overlaid in each CFAD. The azimuthal averaged tangential winds in the inner region (solid) and outer region (dashed) were also overlaid in (e) and (f).

The modal distribution of reflectivity in the outer region extended to an altitude of about 11 km (Fig. 3.10b), whereas the modal distribution of reflectivity in the inner region extended to an altitude of just over 8 km (Fig. 3.10a). The modal distributions demonstrate that convective elements in the inner region were generally shallower than the convective elements in the outer region. However, the lower frequencies of 20 dBZ reflectivity above 8 km in the inner region suggest that deeper convective elements did occur in the inner region. Compared to the narrower modal distribution at weaker reflectivities in the lower levels of the outer region, the modal distribution at the lower levels of the inner region was wider and reached reflectivity values of close to 40 dBZ. An explanation for this difference cannot be offered at this moment. Since understanding the differences in the modal distribution between the inner and outer regions is not key to this study, these differences will be analyzed in future work.

Deep-layer low-level inflow and upper-level outflow dominated the outer region, with the modal distribution showing that inflow was dominant below 4 km altitude (Fig. 3.10d). Below 3 km in the inner region, the frequency of radial velocities were spread between inflow and outflow (Fig. 3.10c). This spread is because of the decreasing outflow height with decreasing radius in the inner region (Fig. 3.9b). There were two other peaks in inflow around 4 km and 8 km altitude. An examination of the individual cross-sections in this leg revealed that the inflow were concentrated on the inner edge of the convective columns (not shown). The mid- and upper-level inflow could be errors in the analysis that resulted from poor radar geometry, or they could be a realistic phenomenon such as the buoyancy-induced pressure gradient acceleration.

The modal distribution of tangential velocities is shallower in the inner region (Fig. 3.10e), which indicate that tangential winds in the inner region were confined to the lower levels. The azimuthal mean tangential wind in the inner region was stronger than the azimuthal mean tangential winds in the outer region (Fig. 3.10e,f). The peak in the mean tangential winds occurred just below 2 km altitude in the inner region and just below 4 km altitude in the outer region. However, the peak in the mean tangential winds in the outer region were of the same strength as that in the inner region at the same altitude.

Observations in the 1853 UTC Leg corroborates some of the observations made by Didlake and Houze (2013a) in a similar convectively-dominant rainband of Hurricane Rita. The height of convection and the depth of the inflow layer decreased with radius. There was also a low-level tangential jet associated with the convective column in the inner region. However, in contrast to the findings

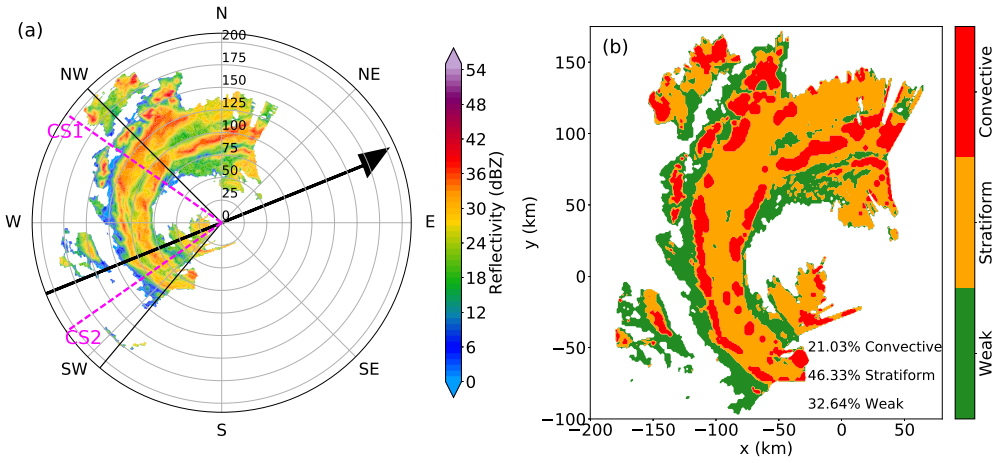

FIG. 3.11. (a) Radar reflectivity field at 2 km altitude with an overlaid arrow indicating the shear heading for the 2018 UTC Leg. The azimuthal angles from which the azimuthally-averaged cross-section was derived are indicated by the two black lines. Individual cross-sections were taken along the dashed magenta lines, labeled CS1 and CS2. (b) The corresponding result of the convective-stratiform algorithm.

of Didlake and Houze (2013a), there was no distinguishable difference in the strength of the inflow between the inner region and the outer region. The difference between the convectively-dominant rainbands of Ophelia and Rita may be indicative of structural difference between storms of different intensities, since Ophelia was a weakening Category 1 storm at the time of the observation while Rita was an intensifying Category 5 storm. Nonetheless, the structure of the azimuthally-averaged variables is undoubtedly one of a convectively-dominant portion of a rainband.

3.3.2 2018 UTC Leg

The 2018 UTC Leg spanned from the downshear left quadrant to the upshear right quadrant, with only the upshear left quadrant being completely occupied by the rainband (Fig. 3.11a). The double-band convection feature seen in the 1853 UTC Leg was also seen in this leg. However, convection was organized in quasi-linear configuration in the 2018 UTC Leg, with stratiform precipitation located in between the two bands of convection (Fig. 3.11b). Based on the convective-stratiform partitioning algorithm, convective activity was also more active in the upwind portion of the 2018 UTC Leg and slowly diminished towards the downwind end of the rainband, where areas of convection significantly declined for the outer region and were more isolated in the inner region (Fig. 3.11b).

In a shear-relative framework, the 2018 UTC Leg is where stratiform precipitation was expected to be dominant (Hence and Houze 2012). The well-organized nature of the convectively-classified

echoes indicated that a larger, stratiform-scale circulation may be dominant in organizing the convection. Nonetheless, there were convectively-classified echoes. The convectively-classified echoes in the inner region may be embedded convection, or are just an artifact of the convective-stratiform partitioning algorithm, which is based solely on the reflectivity field at 2 km altitude. The convective centers in the inner region, as defined by the algorithm, may simply be locally-enhanced precipitation that arose from the larger stratiform-scale circulation. Didlake and Houze (2013b) associated this locally-enhanced precipitation with the rising outflow maximum of the stratiform precipitation. This rising outflow maximum can be strong enough to keep precipitation particles aloft long enough for them to grow larger, thus producing locally-enhanced reflectivity columns that resemble that of reflectivity columns produced from convective updrafts.

As in the 1853 UTC Leg, azimuthal averages of vertical, radial, and tangential winds were generated for the 2018 UTC Leg (Fig. 3.12). Precipitation features at radii smaller than about 50 km and larger than about 150 km did not occur throughout the whole length of the rainband (Fig. 3.11a). Therefore, the following discussion will mainly focus on the kinematic features seen in the rainband between 50 and 150 km radius. In contrast to the double reflectivity column seen in each inner and outer region of the 1853 UTC Leg, each inner and outer region in the 2018 UTC Leg was characterized by a single reflectivity column (Fig. 3.12). Even though the convective-stratiform algorithm classified the precipitation area between the inner and outer convective columns as stratiform, no brightband feature was seen in the azimuthal composite. This is not unusual, however, since the indication of stratiform precipitation is not exclusively tied to the presence of a brightband.

This leg was characterized by the presence of a descending mid-level inflow (Fig. 3.12b). This inflow, which was much shallower than that observed in Hurricane Rita's rainband (Didlake and Houze 2013b), began from radially outside the rainband where the vertical velocities were weakly positive. It continued into the rainband where it split into two branches. A tangential wind maximum was found on the inner edge of the mid-level inflow at approximately 2 km altitude (Fig. 3.12c). However, the whole rainband was associated with a large area of stronger tangential winds relative to the 1853 UTC Leg, with winds over 30 m s^{-1} present in a large portion of the rainband. The two branches of descending mid-level inflow were the result of the data distribution in the azimuthal averaging. The fraction of data points included in the azimuthal averaging at the outer descending mid-level inflow branch is less than half (Fig. 3.13b). Thus, the outer branch of the descending mid-level inflow is not representative of the whole rainband and is partially a product of the azimuthal averaging.

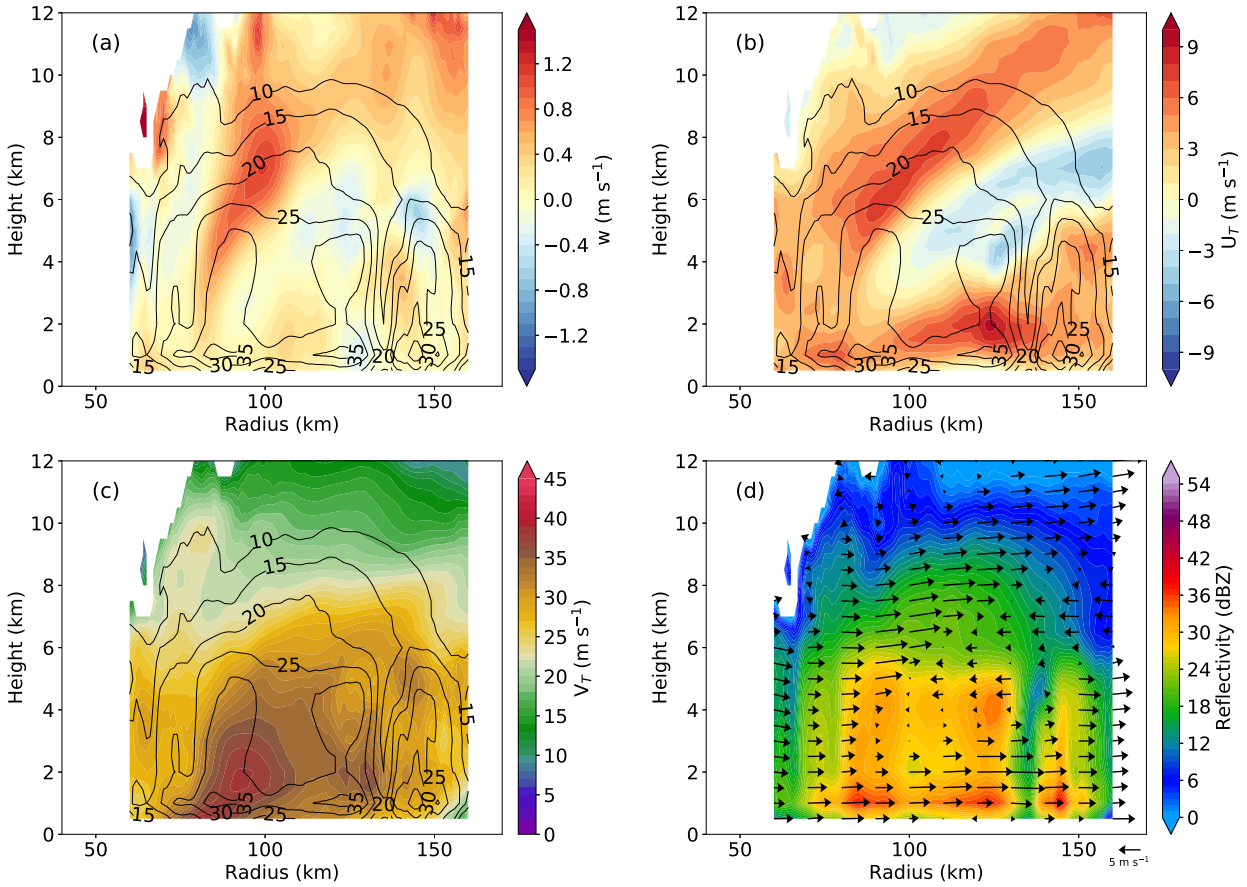

FIG. 3.12. Azimuthally-averaged (a) vertical, (b) radial and (c) tangential velocities (m s^{-1}) with overlaid contours of azimuthally-averaged reflectivity (dBZ), and (d) the azimuthally-averaged reflectivity (dBZ) with overlaid wind vectors in the 2018 UTC Leg.

To investigate the azimuthal differences in the rainband structure, individual cross-sections at different azimuths were taken from the upwind and downwind portion of the rainband (dashed magenta line in Fig. 3.11a), labeled as CS1 and CS2, respectively. The mid-level inflow at CS1 was much stronger than the mid-level inflow at CS2 (Fig. 3.14b,d). The tangential winds showed similar changes in strength, with stronger tangential winds observed at CS1 than at CS2. In essence, the stratiform mid-level inflow weakened from the upwind portion to the downwind portion of the rainband. Following the weakening inflow was a weakening in the tangential winds.

Rising outflow was found above the inner edge of the descending inflow (Fig. 3.12a,b). This rising outflow was also collocated with the top of the inner reflectivity column. There was also another region of rising outflow beneath the descending mid-level inflow. These features are in agreement with the observations made by Didlake and Houze (2013b) of the stratiform portion of Hurricane Rita's rainband. The mid-level inflow, and rising outflow above and beneath it also concur with that observed

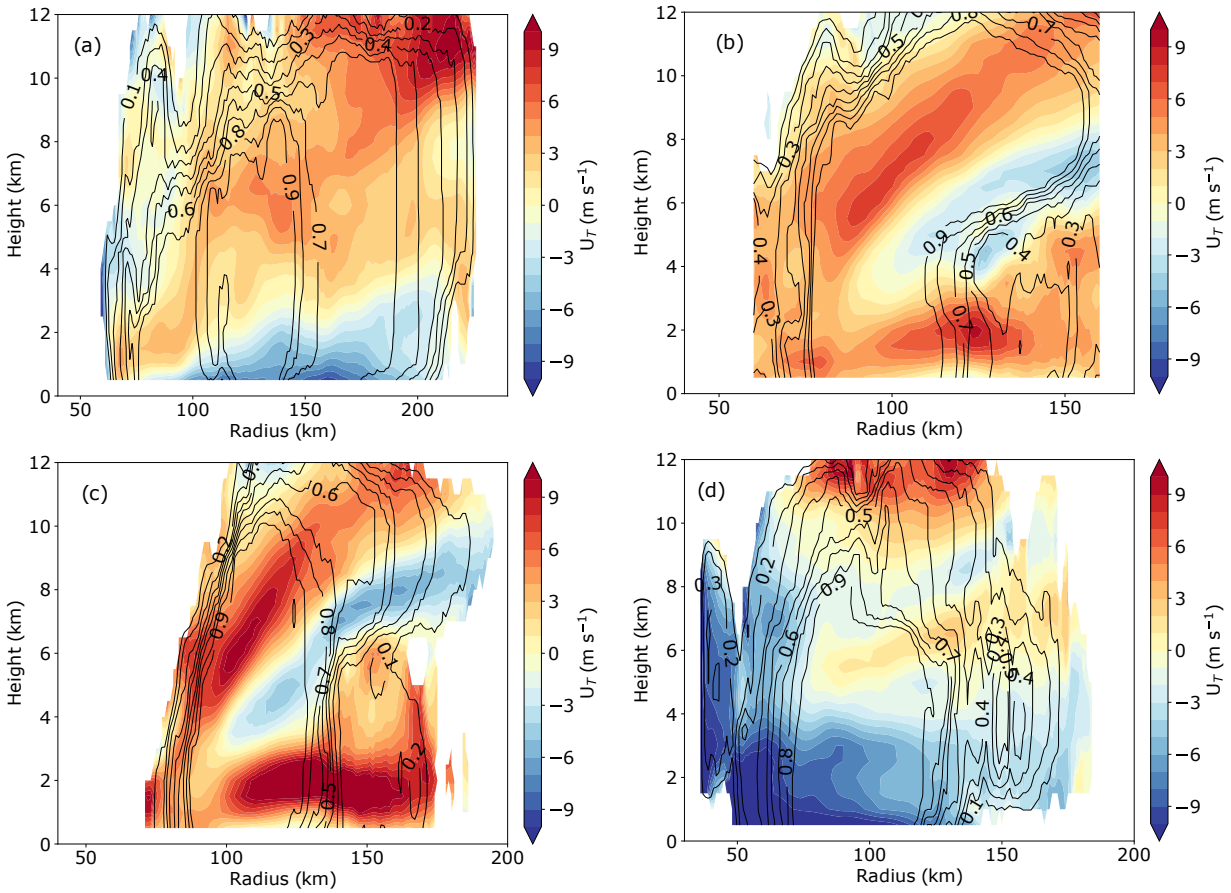

FIG. 3.13. Azimuthally-averaged radial winds overlaid with fraction of datapoints included in the azimuthal averaging for the (a) 1853 UTC, (b) 2018 UTC, (c) 2133 UTC, and (d) 2154 UTC Legs.

from the idealized simulation of stratiform heating in the rainband by Moon and Nolan (2010). The inner reflectivity column appeared consistently with the presence of the stratiform mid-level inflow when individual cross-sections were analyzed (not shown). Thus, the inner reflectivity column is most likely associated with the larger stratiform-scale circulation and not by embedded convection. The rising outflow beneath the mid-level inflow may be the supergradient response to the tangential wind maximum located on its inner edge. Similar to the 1853 UTC Leg, the reflectivity column in the outer region of the 2018 UTC Leg did not seem to be associated with any specific feature of the rainband kinematics.

3.3.3 2133 UTC Leg

The 2133 UTC Leg was located in a similar location as the 2018 UTC Leg, with a slight downwind shift. As such, the 2133 UTC Leg was located in both upshear quadrants (Fig. 3.15a). The observation period for the 2133 UTC Leg began approximately 20 minutes after the observation of the 2018 UTC

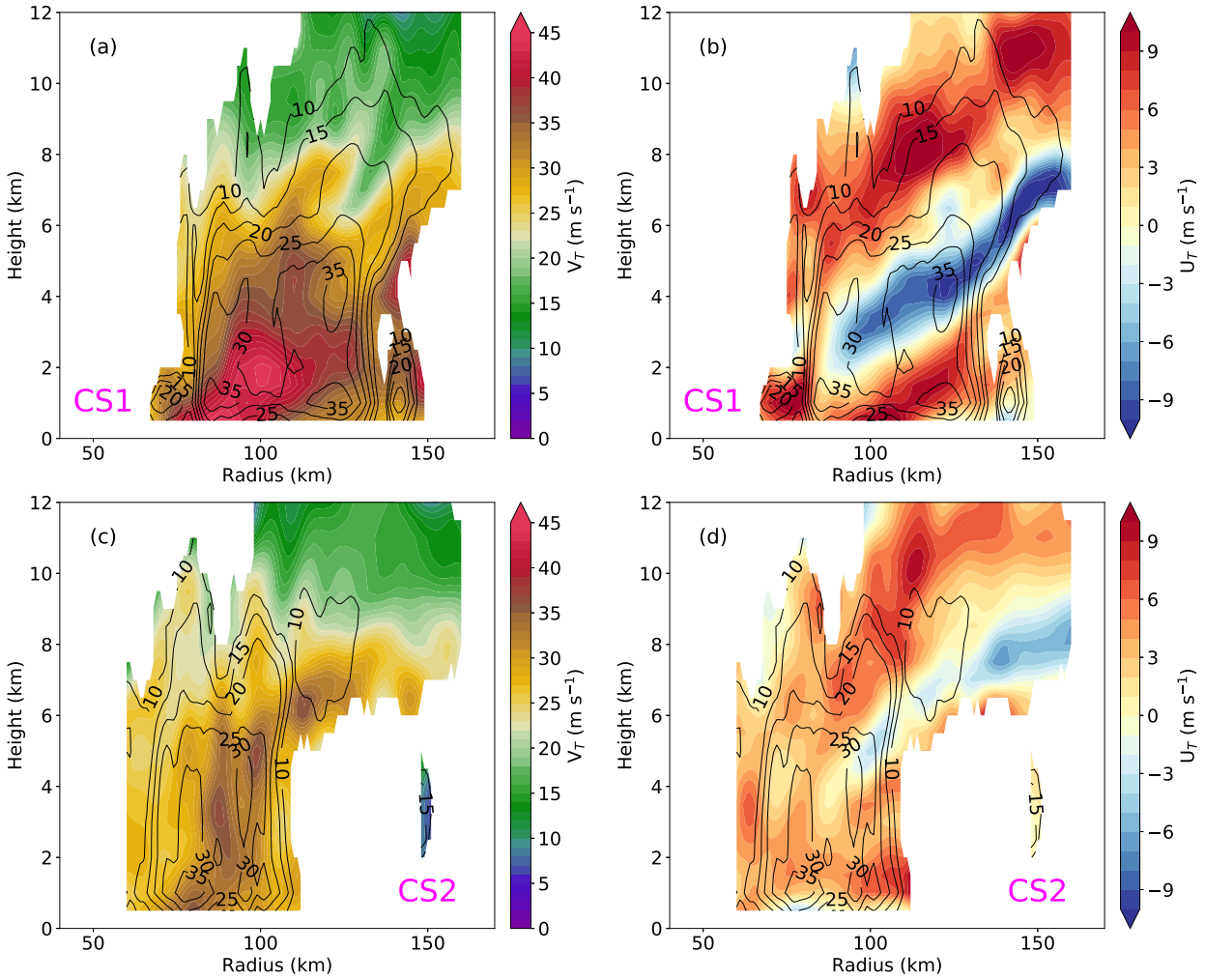

FIG. 3.14. Individual cross-sections of tangential velocity (left column; m s^{-1}) and radial velocity (right column; m s^{-1}) in the 2018 UTC Leg. Overlaid are contours of reflectivity (dBZ). The location of the cross-sections (CS) correspond to the lines labeled in Fig. 3.11a

Leg had ended. In the outer region of the 2133 UTC Leg, convective-classified echoes were dominant in the upwind portion of the rainband and became diminished towards the downwind end, similar to that seen in the 2018 UTC Leg (Fig. 3.15b). Convective echoes in the inner region, however, were weaker in the upwind end and stronger in the downwind end - the reverse of what was observed in the 2018 UTC Leg. The additional areas of convective echoes in the downwind portion of the 2133 UTC Leg, beyond that observed in the 2018 UTC Leg, resulted in a slight increase in the fraction of convective-classified echoes.

Since the 2018 UTC Leg and the 2133 UTC Leg were located in approximately the same region, a deliberate effort was made to generate azimuthal averages over the same arc in both legs (Fig. 3.11a,

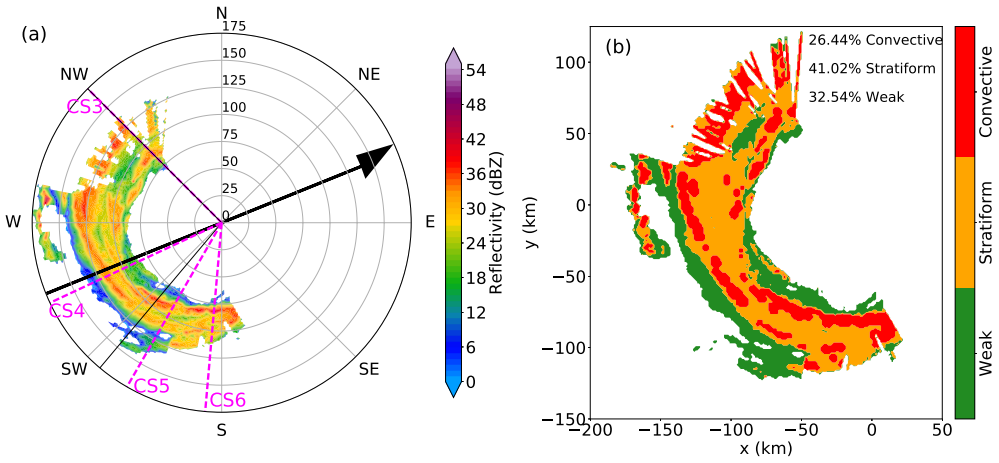

FIG. 3.15. (a) Radar reflectivity field at 2 km altitude with an overlaid arrow indicating the shear heading for the 2133 UTC Leg. The azimuthal angles from which the azimuthally-averaged cross-section was derived are indicated by the two black lines. Individual cross-sections were taken along the dashed magenta lines, labeled CS3, CS4, CS5, and CS6. (b) The corresponding result of the convective-stratiform algorithm.

3.15a) . This allows for a time-evolution analysis as opposed to an upwind-vs-downwind comparison. The azimuthal averages of the vertical, radial, and tangential winds for the 2133 UTC Leg are depicted in Fig. 3.16. The kinematic features of the 2018 UTC Leg were enhanced in the 2133 UTC Leg. In the azimuthally-averaged view, the descending mid-level inflow was better defined and stronger, with enhancements of similar magnitude seen in the rising outflow above and beneath the inflow (Fig. 3.16a,b). The single mid-level inflow branch observed in this leg is representative of the circulation along the arc of the rainband, as the fraction of data points over which these features were averaged is over 0.9 (Fig. 3.13c). The inner reflectivity column seen in the 2018 UTC Leg had dissipated in the 2133 UTC Leg. Yet, updraft and outflow maxima could still be found at approximately the same radius.

The tangential wind maximum had also intensified, and appeared more concentrated with a center at around 100 km radius and 2 km altitude (Fig. 3.16c). Strong winds of similar strength to the tangential wind maximum extended up to an altitude of 4 km. The outer reflectivity column did not appear to be associated with any azimuthally-averaged rainband kinematics. Individual cross-sections were analyzed to investigate the kinematic structure along the arc of the rainband. These cross-sections are labeled in Fig. 3.15a. CS3 and CS4 are the respective upwind and downwind cross-sections of this leg. CS5 and CS6 are cross-sections beyond that analyzed in the azimuthal average, where the rainband transitioned from being stratiform-dominant to what we hypothesize is a developing secondary eyewall.

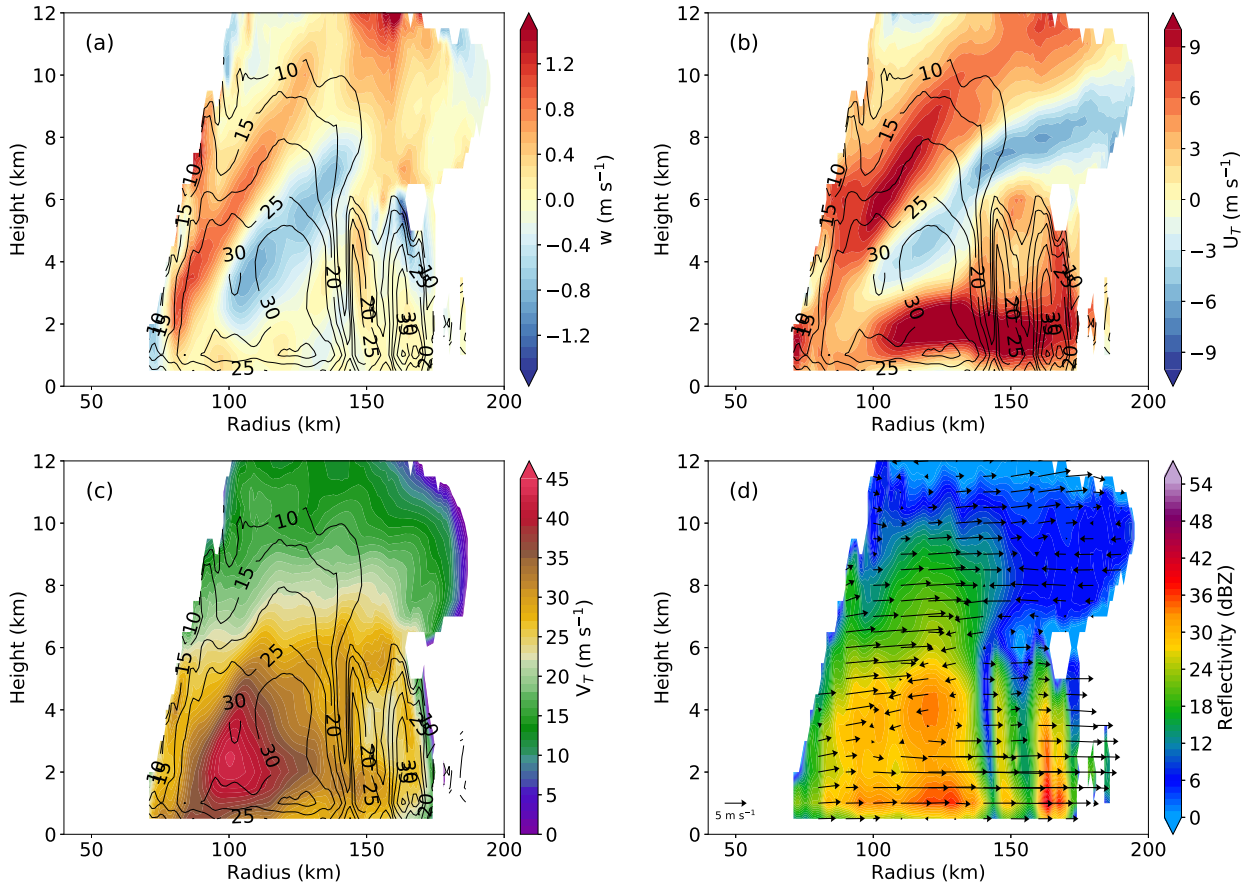

FIG. 3.16. Azimuthally-averaged (a) vertical, (b) radial and (c) tangential velocities (m s^{-1}) with overlaid contours of azimuthally-averaged reflectivity (dBZ), and (d) the azimuthally-averaged reflectivity (dBZ) with overlaid wind vectors in the 2133 UTC Leg.

The enhancement of the stratiform circulation from the 2018 UTC Leg to the 2133 UTC Leg is evident in CS3 and CS4 (Fig. 3.17a,b,c,d). The mid-level inflow in CS3 (Fig. 3.17b) is much deeper than the mid-level inflow observed in the upwind portion of the 2018 UTC Leg (CS1; Fig. 3.14b). Similarly, the mid-level inflow in CS4 (Fig. 3.17d) is stronger than that in CS2 (Fig. 3.14d). Note that a low-level inflow was beginning to form in CS4 (Fig. 3.17d). Further downwind, the kinematics associated with the stratiform precipitation began to transition into a more convectively-dominant kinematics of lower-level inflow and upper-level outflow. The stratiform mid-level inflow began to weaken at CS5, before merging with low-level inflow to form a deep-layer inflow at CS6. Similar to the 2018 UTC Leg, the strength of the tangential winds in the 2133 UTC Leg were correlated to the strength of the mid-level inflow. As the stratiform mid-level inflow weakened from CS3 to CS6, so did the strength of the tangential winds (Fig. 3.17).

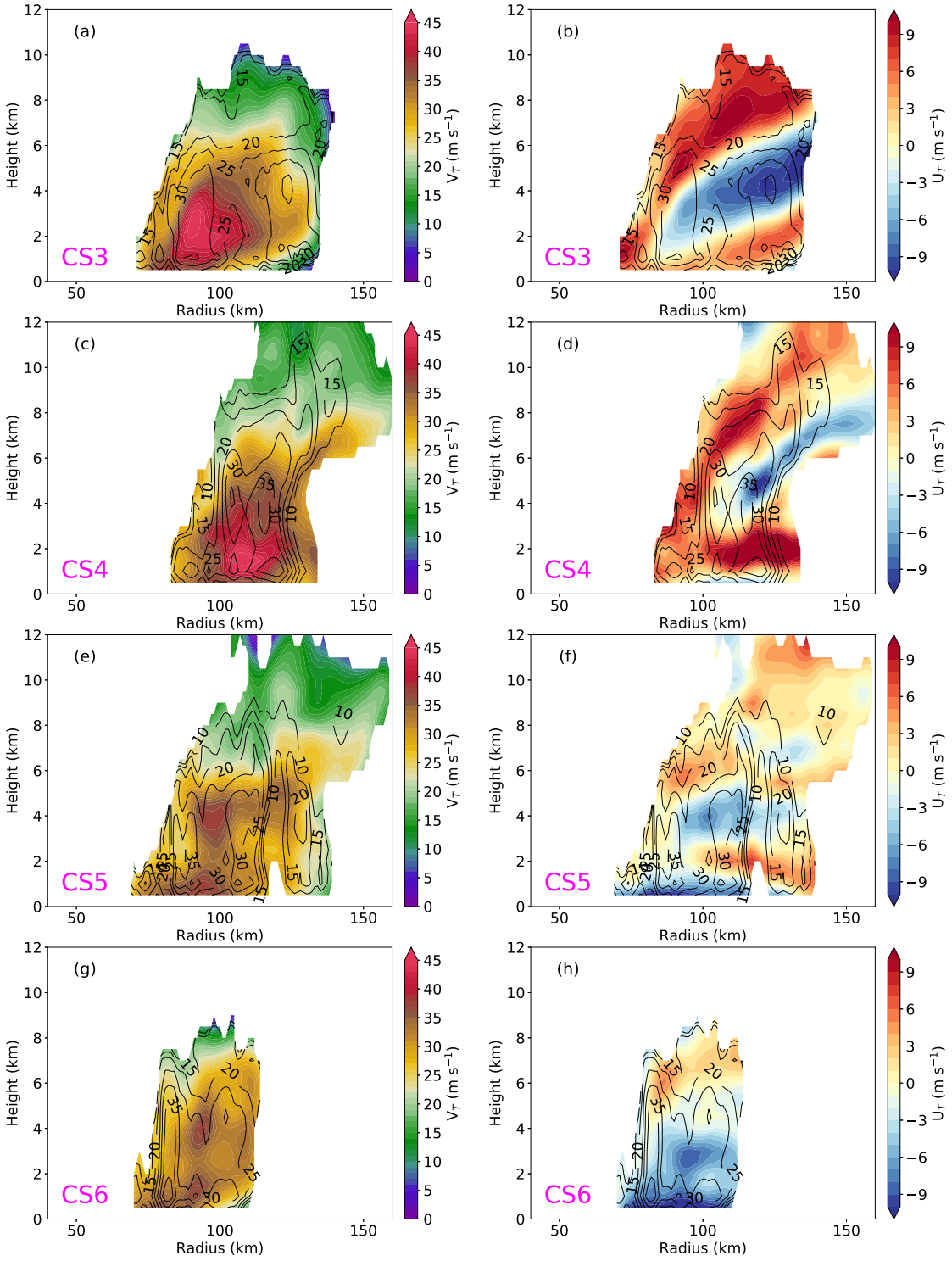

FIG. 3.17. Individual cross-sections of tangential velocity (left column; m s^{-1}) and radial velocity (right column; m s^{-1}) in the 2133 UTC Leg. Overlaid are contours of reflectivity (dBZ). The location of the cross-sections (CS) correspond to the lines labeled in Fig. 3.15a

The 2133 UTC Leg exhibited an enhancement in stratiform rainband kinematics compared to the 2018 UTC Leg. The strength of the mid-level inflow and tangential winds in both the upwind and downwind portions of the 2133 UTC Leg were stronger than that seen in the 2018 UTC Leg. Where the stratiform mid-level inflow was strong, the tangential winds on the inner edge of the inflow were also strong. Further downwind of the 2133 UTC Leg, the stratiform rainband kinematics weakened and transitioned into a low-level inflow and upper-level outflow pattern typically associated with convective precipitation.

3.3.4 2154 UTC Leg

The 2154 UTC Leg was located in the right-of-shear quadrants of Ophelia (Fig. 3.18a). The 2154 UTC Leg was also the portion of the rainband closest to the inner core out of the four rainbands analyzed in this study, appearing between 50 and 125 km radius. The double band convection feature seen in the previous three legs was absent in this leg (Fig. 3.18b). The inner region consisted of convective-classified echoes that continued from the 2133 UTC Leg. In the outer region, patches of convective echoes located south of the eye between 125 and 150 km radius spiraled inward and merged with the inner region at approximately 75 km radius to the southeast of the eye. There was no apparent difference in convective echoes between the upwind region and downwind region of the 2154 UTC Leg.

Azimuthal averages of the vertical, radial, and tangential winds of the 2154 UTC Leg are shown in Fig. 3.19. A deep layer of low-level rising inflow was observed in the 2154 UTC Leg, with the depth of the inflow layer extended up to 5 km altitude (Fig. 3.19,b). Immediately above this inflow layer and radially outside the rainband, an outflow layer was observed. Above this outflow layer at approximately 8 km altitude, a weak and shallow inflow layer existed. This feature is the remnant mid-level inflow seen in the 2018 UTC and 2133 UTC Legs. Higher up, another region of outflow was seen. The deep inflow layer seen in this leg is opposite to what was observed in a similar downwind portion of Hurricane Rita's rainband, which was characterized by radial outflow throughout the depth of the rainband with disorganized vertical velocity profile (cf. Fig. 10 in Didlake and Houze 2013b).

The corresponding tangential wind profile was of enhanced tangential winds throughout the whole rainband region, which extended up to 6 km altitude (Fig. 3.19c). There were two regions of stronger tangential winds: one at around 100 km radius and 4 km altitude, and another at around 75 km radius and 1.5 km altitude. The radial and tangential wind profiles of the 2154 UTC Leg seems to be a combination of the convective-dominant (1853 UTC Leg) and stratiform-dominant (2018 UTC and 2133 UTC Legs) portions of Ophelia's rainband. However, the deep inflow layer associated with the

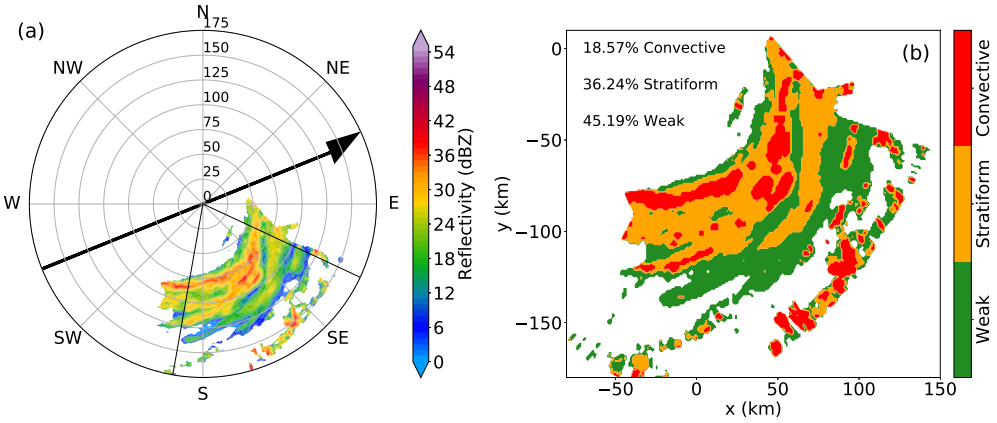

FIG. 3.18. (a) Radar reflectivity field at 2 km altitude with an overlaid arrow indicating the shear heading for the 2154 UTC Leg. The azimuthal angles from which the azimuthally-averaged radial cross-section was derived are indicated by the two black lines. (b) The corresponding result of the convective-stratiform algorithm.

in-up-out secondary circulation, and the single convective tower located on the inner edge of the rainband indicated that this portion of the rainband is convectively-dominant. We hypothesize that this convectively-dominant rainband is the developing secondary eyewall associated with Ophelia's ERC.

To summarize, the 1853 UTC Leg was part of the convectively-dominant outer rainbands of Hurricane Ophelia and was associated with relatively weak low-level tangential wind maximum. The 2018 UTC Leg and the 2133 UTC Leg were the stratiform-dominant rainbands and were associated stronger tangential wind maximum in the low- to mid-levels. An enhancement in the stratiform kinematics was observed between the 2018 UTC Leg and the 2133 UTC Leg. Downwind of the 2133 UTC Leg, the stratiform kinematics transitioned into convectively-dominant kinematics in the 2154 UTC Leg. This convectively-dominant 2154 UTC Leg is hypothesized to be the developing secondary eyewall in Ophelia's ERC.

The 85-GHz satellite microwave imagery captured around the time the research flights were conducted provided further evidence to the airborne radar observations. Just before the 1853 UTC Leg, deep convection was active in the outer rainbands of Hurricane Ophelia (Fig. 3.20a). The location of this deep convection is in the approximate location of the 1853 UTC Leg. Convection in the location of the 2018, 2133, and 2154 UTC Legs were weak. After the conclusion of the research flight, overall rainband convection had diminished (Fig. 3.20c). However, shallow convection was still present and was observed in the 37-GHz satellite microwave imagery (Fig. 3.20b). In the 37-GHz image, shallow eyewall convection was "opened" to the southwest. Outside the eyewall, a moat - a relatively precipitation-free

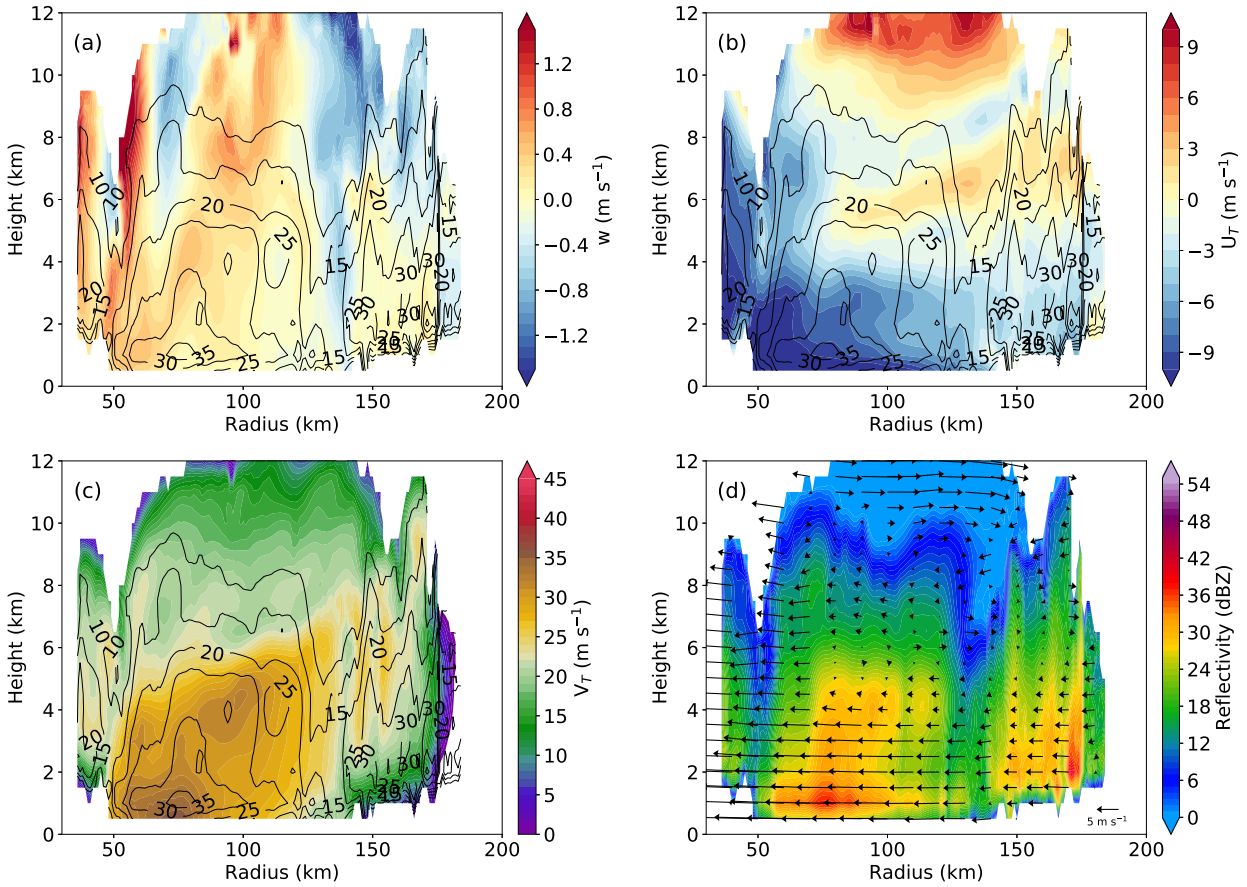

FIG. 3.19. Azimuthally-averaged (a) vertical, (b) radial and (c) tangential velocities (m s^{-1}) with overlaid contours of azimuthally-averaged reflectivity (dBZ), and (d) the azimuthally-averaged reflectivity (dBZ) with overlaid wind vectors in the 2154 UTC Leg.

region - had formed in arc that extended from the west to the south. Radially outside of this moat were the 2018, 2133, and 2154 UTC Legs. The image resembles that of a secondary eyewall made up of the 2018, 2133, and 2154 UTC Legs and thus, serving as strong evidence that the 2154 UTC Leg was a developing secondary eyewall.

3.4 ABSOLUTE ANGULAR MOMENTUM (AAM) BUDGET

To understand how the secondary circulation of Ophelia's rainbands may contribute to the spin-up of the storm's tangential winds, an absolute angular momentum (AAM) budget was calculated using the flux form of the azimuthally-averaged tangential momentum equation in cylindrical coordinates.

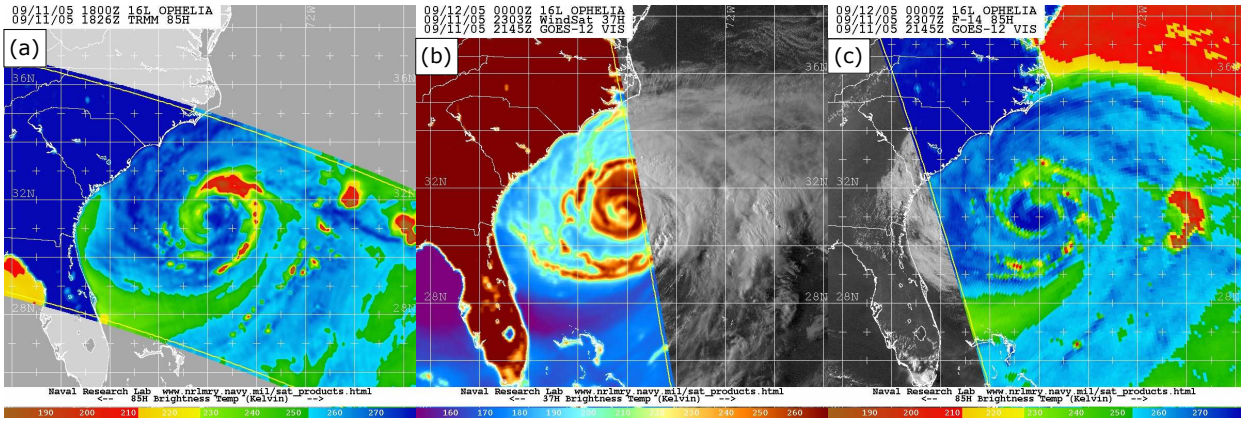

FIG. 3.20. (a) 85-GHz microwave imagery of Hurricane Ophelia at the start of the research flights, and (b) 37-GHz and (c) 85-GHz microwave imagery of Hurricane Ophelia after the conclusion of the research flights on the 11$^{\text{th}}$ of September.

Assuming that the frictional torques are negligible in the free troposphere above the TC boundary layer, the azimuthally-averaged AAM flux divergence equation can be written as:

$$\frac{\partial(\rho M)}{\partial t} + \frac{\partial(\rho r u M)}{r \partial r} + \frac{\partial(\rho w M)}{\partial z} = 0$$

$$\text{Where } M = r v + \frac{1}{2} f r^2$$

Here, M is the absolute angular momentum, r is the radius from the center of the storm, v is the tangential wind, f is the Coriolis parameter $2\Omega \sin\theta$, where the reference latitude $\theta = 31°\text{N}$ was used, and ρ is the air density retrieved from SAMURAI's output, which used the Dunion moist tropical sounding (Dunion 2011) as its reference state. u and w are the respective radial and vertical winds.

A common practice in budget analyses is to further separate each term into an azimuthal mean and perturbation quantity, such that $x = \overline{x} + x'$ where x represents the ρ, u, v, w, and M terms. However, the spatial and temporal resolution of the dataset used herein was not sufficient to resolve the perturbation terms. Therefore, the AAM budget analysis was done in the context of the time-average azimuthal mean terms alone, with a focus on fluxes above the boundary layer where friction is negligible. Note that the sign and magnitude of the eddy terms are unknown, but they can have a non-negligible effect on the total tendency. The radial and vertical flux divergence calculated in all the legs occurred in near-cancellation such that the total tendency field is near-zero (not shown). Without a complete measurement of the eddy fluxes, the total tendency field could not be completely resolved as the budget cannot be closed.

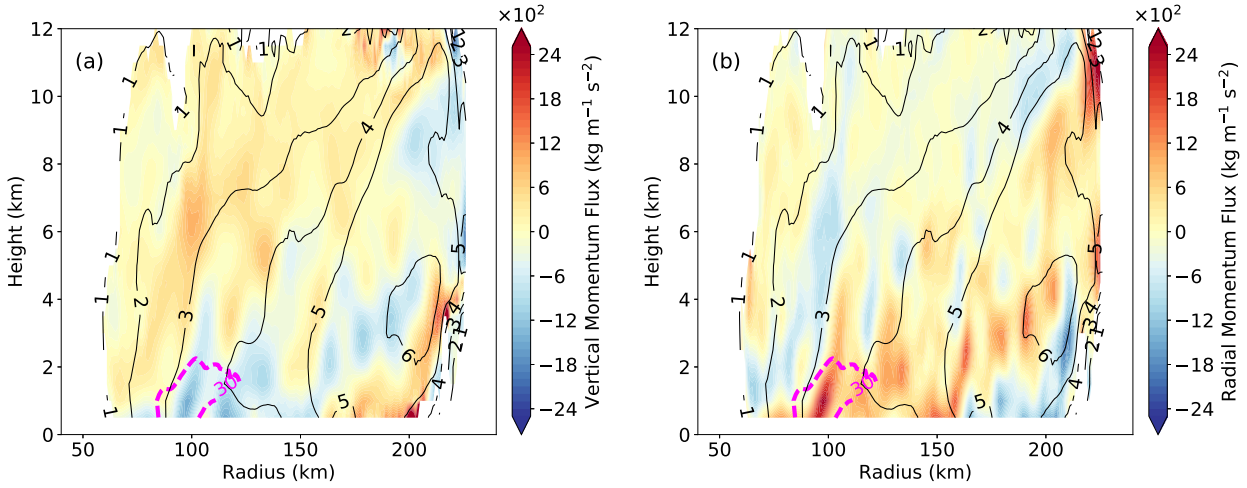

FIG. 3.21. (a) Vertical and (b) radial flux of absolute angular momentum calculated from the 1853 UTC Leg. Overlaid are contours of azimuthally-averaged absolute angular momentum ($\times 10^6$ m^2 s^{-1}; solid black) and contours of 30, 35, and 40 m s^{-1} tangential winds (dashed magenta).

Nonetheless, the key factor in this discussion is the relative magnitude of the azimuthally-averaged advective terms in the different portions of the rainband. The vertical and radial flux divergence of AAM for each of the four legs analyzed above are shown in Figs. 3.21-3.24. While the rainbands were associated with coherent radial and vertical velocity features, the regions immediately outside the rainbands were associated with transient radial and vertical velocity features. Thus, the resultant budget analyses outside the rainbands were noisy, and would not be the focus of the following discussion.

In the 1853 UTC Leg, the radial flux convergence of AAM was strongest in the lower levels, and was associated with the inward advection of higher AAM air from the outer radii by the low-level inflow (Fig. 3.21b). Meanwhile, the strongest vertical flux convergence of AAM was located above 4 km altitude, and was associated with the strongest upward vertical velocities observed in this leg (Fig. 3.22a). Below 4 km altitude, flux divergence of AAM was produced by updrafts that advected lower AAM air upward. The low-level radial flux convergence of AAM was almost completely balanced by the low-level vertical flux divergence of AAM, while the upper-level flux convergence of AAM was located in a region with near-zero radial flux divergence of AAM.

The 2018 UTC Leg was associated with a low-level radial flux divergence of AAM by the supergradient outflow (Fig. 3.22b). In the mid-to-upper-levels, a prominent region of radial flux convergence of AAM was seen, and was associated with the inward advection of higher AAM air by the stratiform mid-level inflow (Fig. 3.12b). Radially inside of the stratiform mid-level inflow, the rising stratiform mid-level outflow produced a flux divergence of AAM (Fig. 3.22a). Conversely, rising supergradient

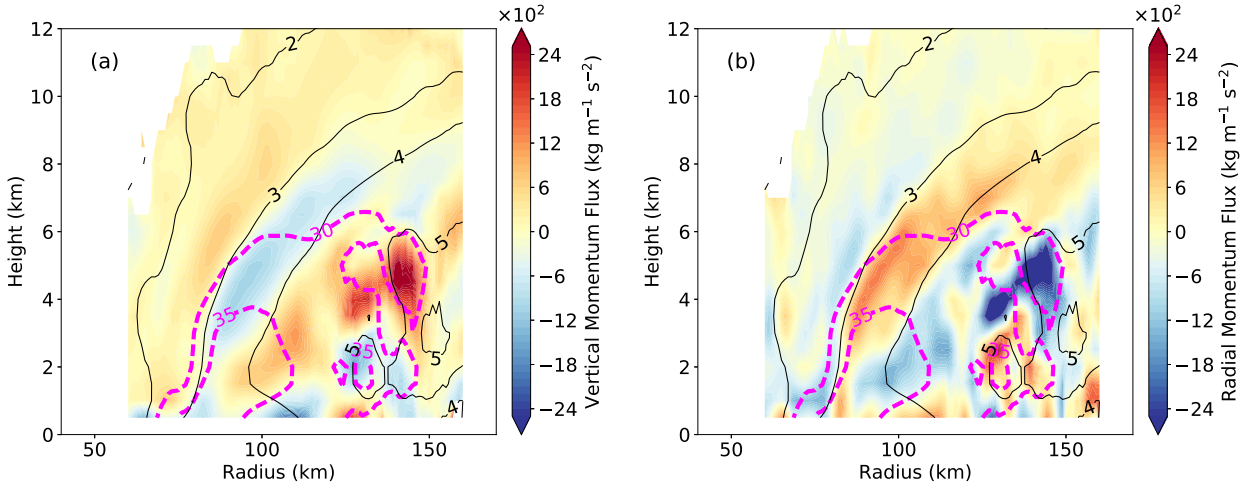

FIG. 3.22. (a) Vertical and (b) radial flux of absolute angular momentum calculated from the 2018 UTC Leg. Overlaid are contours of azimuthally-averaged absolute angular momentum ($\times 10^6$ m^2 s^{-1}; solid black) and contours of 30, 35, and 40 m s^{-1} tangential winds (dashed magenta).

outflow in the low-levels was associated with a vertical flux convergence of AAM. Similarly, the rising stratiform mid-level outflow was also associated with a vertical flux convergence of AAM, while the descending stratiform mid-level inflow was associated with a vertical flux divergence of AAM.

Since the 2133 UTC Leg was over the same stratiform-dominant region as the 2018 UTC Leg, the momentum fluxes observed in the 2133 UTC Leg were generally similar in structure to that observed in the 2018 UTC Leg. Radial flux convergence of AAM was associated with the mid-level inflow while radial flux divergence was associated with the stratiform mid-level outflow and low-level supergradient outflow (Fig. 3.23b). The descending mid-level inflow was associated with a vertical flux divergence of AAM, while the rising stratiform mid-level outflow and rising supergradient outflow contributed to a vertical flux convergence of AAM (Fig. 3.23a). The stronger AAM fluxes in this leg compared to the 2018 UTC Leg is associated with the enhancement in the stratiform kinematics, as discussed in the previous chapter.

The momentum budget analysis of the 2154 UTC Leg was similar in structure to the 1853 UTC Leg, but with generally weaker fluxes. The radial flux of AAM was weakly convergent below 5 km altitude, with near-zero fluxes above (Fig. 3.24b). Meanwhile, the reverse was true for the vertical fluxes of AAM (Fig. 3.24a). Even though the 2154 UTC Leg was characterized by deeper and slightly stronger inflow (Fig. 3.19b), the radial fluxes of AAM were weaker in the 2154 UTC Leg compared to the 1853 UTC Leg. The weaker radial flux of AAM in the 2154 UTC leg is because of the weaker radial gradient in AAM compared to the 1853 UTC Leg.

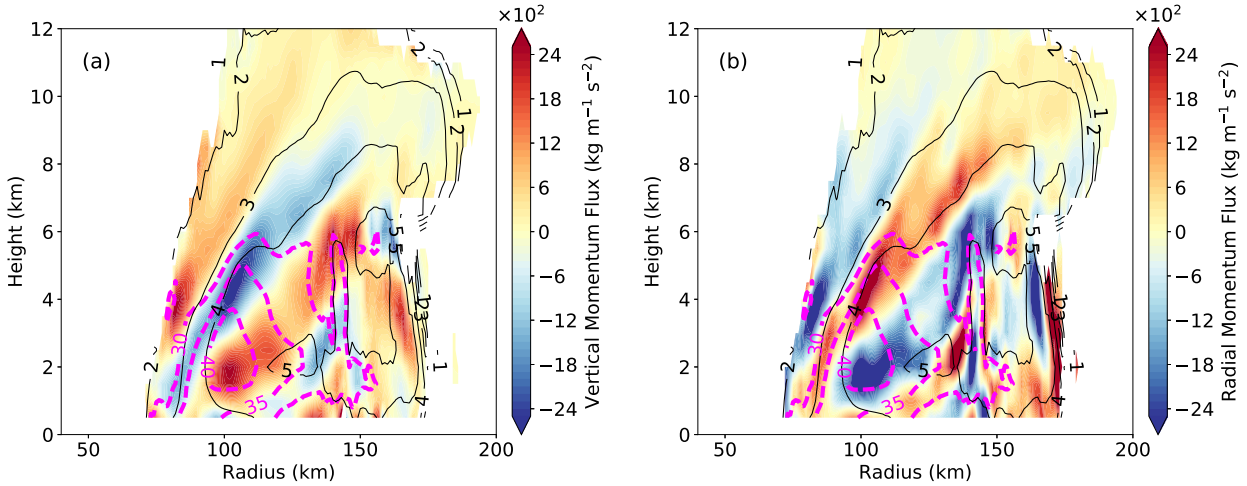

FIG. 3.23. (a) Vertical and (b) radial flux of absolute angular momentum calculated from the 2133 UTC Leg. Overlaid are contours of azimuthally-averaged absolute angular momentum ($\times 10^6$ m^2 s^{-1}; solid black) and contours of 30, 35, and 40 m s^{-1} tangential winds (dashed magenta).

The momentum budget analyses showed that the strongest radial flux convergence of AAM was associated with the mid-level inflow in stratiform-dominant rainbands, where the strongest low- to mid-level tangential winds were also observed. The concomitance of the strongest radial flux convergence of AAM and the strongest tangential winds suggests a direct relationship between them. This inference is further supported by the correlation between the location of the enhanced tangential winds and the location of the local maximum in the radial momentum flux convergence. Enhanced tangential winds occurred in the low-levels when the local maximum in the radial momentum flux convergence was concentrated in the low levels (Fig. 3.21), while enhanced tangential winds occurred in the mid-levels when the local maximum in the radial momentum flux convergence was concentrated in the mid-levels (Figs. 3.22,3.23). Where there was a deep region of positive radial momentum flux convergence associated with the deep inflow of the 2154 UTC Leg, a deep area of enhanced tangential winds were observed (Fig. 3.24).

However, the true nature of this relationship cannot be completely understood due to the near-cancellation of the radial and vertical flux divergence of AAM that results in a near-zero tendency, and because of the unresolved eddy fluxes in the AAM budget that could affect the sign of the tendency. Nonetheless, the analyses support our hypothesis in that strong radial flux of AAM is associated with the mid-level inflow in the stratiform-dominant portion of the TC rainband.

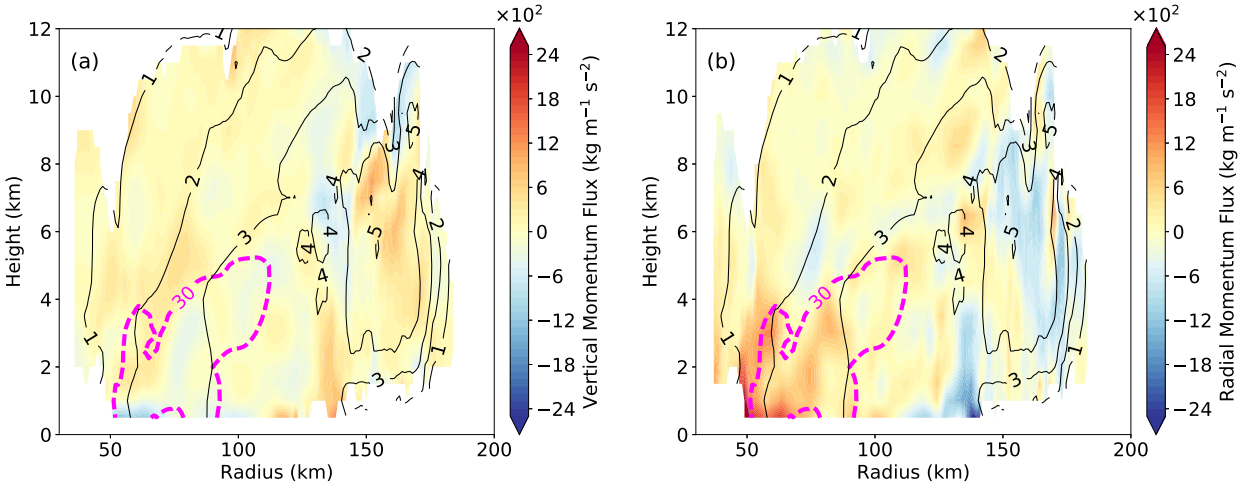

FIG. 3.24. (a) Vertical and (b) radial flux of absolute angular momentum calculated from the 2154 UTC Leg. Overlaid are contours of azimuthally-averaged absolute angular momentum ($\times 10^6$ m^2 s^{-1}; solid black) and contours of 30, 35, and 40 m s^{-1} tangential winds (dashed magenta).

CHAPTER 4

CONCLUSION

Hurricane Ophelia (2005) underwent an unconventional eyewall replacement cycle (ERC) in that the ERC occurred while Ophelia was a weak Category 1 hurricane located over cold sea surface temperatures. Using the flight-level dataset from USAF aircraft hurricane reconnaissance missions into Ophelia, the flight-level tangential wind field was shown to evolve similarly to a storm undergoing a conventional ERC, with the corresponding satellite microwave imagery showing a similar evolution in convective activity. However, neither concentric eyewalls, nor a complete circular eyewall was apparent in the satellite microwave imagery.

The weakening phase of Ophelia's ERC - during which a secondary wind maximum typically intensifies - on 11 September 2005 was observed as part of the Hurricane Rainband and Intensity Change Experiment (RAINEX). Airborne radar data were obtained from the Naval Research Laboratory (NRL) and the National Oceanic and Atmopheric Administration (NOAA) P-3 aircraft that flew simultaneously along a rainband, allowing for quad-Doppler wind retrievals of rainband kinematics. A spline-based three-dimensional variational wind synthesis tool known as SAMURAI (Bell et al. 2012) was used in the Doppler wind retrievals. The analyses were conducted in Cartesian coordinates, but were transformed into cylindrical coordinates to allow for an azimuthally-averaged view of the rainbands.

The distant rainbands of Hurricane Ophelia were characterized by dominantly convective precipitation, with a kinematic structure of low-level inflow and upper-level outflow. A tangential wind maximum was found in the lower levels of the rainband inner region, but was relatively weak. The observations made in this convectively-dominant distant rainband generally corroborate observations in previous studies of convectively-dominant rainbands. The stratiform-dominant portion of Ophelia's rainbands was characterized by a descending mid-level inflow, with rising outflow above and beneath it. A low- to mid-level tangential wind maximum was found on the inner edge of the mid-level inflow. Observations made in the stratiform-dominant rainbands also corroborate observations made in previous studies.

In a time evolution analysis and in upwind-vs-downwind comparisons, the strength of the tangential winds was shown to be correlated with the strength of the stratiform mid-level inflow, where a stronger mid-level inflow was usually associated with stronger tangential winds. Downwind of the

stratiform-dominant rainbands, rainband kinematics gradually transitioned into being convectively-dominant, with a low-level deep-layer inflow and upper-level outflow. We hypothesized that this convectively-dominant rainband is the developing secondary eyewall.

Momentum budget analyses showed that the strongest radial flux convergence of absolute angular momentum (AAM) was associated with the stratiform mid-level inflow, where the strongest tangential winds were also found. In addition, there was a correlation between the location of the enhanced tangential winds with the location of the local maximum in radial momentum flux convergence. However, a direct relationship between the radial fluxes of AAM and the time tendency of the tangential winds cannot be determined due to (i) the near-cancellation of the radial flux of AAM with the vertical flux of AAM, and (ii) the unresolved eddy fluxes in the momentum budget. Nonetheless, the budget analyses suggest that stratiform-dominant rainbands may have played a dominant role in broadening the tangential wind field of Hurricane Ophelia during its ERC. The stratiform-dominant rainbands were hypothesized to have played a dominant role because Ophelia was located over convection-inhibiting cold sea surface temperatures, and because of the areal prominence of the stratiform-dominant rainbands and their close proximity to the inner core (Didlake and Houze 2013b).

However, our hypothesis does not dismiss the role of deep convection in Ophelia's ERC, since convection was re-invigorated as the storm moved over warmer SSTs in the the storm's intensification phase. Neither does this hypothesis suggest that stratiform-dominant rainbands were the sole mechanism through which the broadening of the tangential wind field and the subsequent ERC could occur. Rather, stratiform-dominant rainbands may have played a more significant role in this particular scenario due to the weaker storm and colder SSTs.

While the broadening of the tangential winds has been shown to be associated with the stratiform-dominant portion of Ophelia's rainbands, the manner in which the broadening of the tangential winds initiate or influence Ophelia's ERC is still unknown and is the subject of further research. The relative contributions of rainband convective and stratiform kinematics in a conventional eyewall replacement cycle also warrants further investigation. More importantly, an investigation is needed to understand if the observed rainband kinematics are properly represented either in idealized or operational numerical weather models, which could affect how the model represents TC intensity change.

REFERENCES

Banzon, V., T. M. Smith, T. M. Chin, C. Liu, and W. Hankins, 2014: A long-term record of blended satellite and in situ sea-surface temperature for climate monitoring, modeling and environmental studies. *Earth Syst. Sci. Data*, **8**, 165–176, doi: 10.5194/essd-8-165-2016.

Barnes, G. M., E. J. Zipser, D. Jorgensen, and F. Marks, Jr., 1983: Mesoscale and convective structure of a hurricane rainband. *J. Atmos. Sci.*, **40**, 2125–2137, doi: 10.1175/1520-0469(1983)040<2125:MACSOA>2.0.CO;2.

Bell, M. M., W.-C. Lee, C. A. Wolff, and H. Cai, 2013: A Solo-based automated quality control algorithm for airborne tail Doppler radar data. *J. Appl. Meteor. Climatol.*, **52**, 2509–2528, doi: 10.1175/JAMC-D-12-0283.1.

Bell, M. M., M. T. Montgomery, and K. A. Emanuel, 2012: Air-sea enthalpy and momentum exchange at major hurricane wind speeds observed during CBLAST. *J. Atmos. Sci.*, **69**, 3197–3222, doi: 10.1175/JAS-D-11-0276.1.

Dare, R. A. and J. L. McBride, 2011: The threshold sea surface temperature condition for tropical cyclogenesis. *J. Climate*, **24**, 4570–4576, doi: 10.1175/JCLI-D-10-05006.1.

DeMaria, M., M. Mainelli, L. K. Shay, J. A. Knaff, and J. Kaplan, 2005: Further improvements to the statistical hurricane intensity prediction scheme SHIPS. *Wea. Forecasting*, **20**, 531–543, doi: 10.1175/WAF862.1.

DeMaria, M., C. R. Sampson, J. A. Knaff, and K. D. Musgrave, 2014: Is tropical cyclone intensity guidance improving? *Bull. Amer. Meteor. Soc.*, **95**, 387–398, doi: 10.1175/BAMS-D-12-00240.1.

Didlake, A. C., Jr. and R. A. Houze, Jr., 2009: Convective-scale downdrafts in the principal rainband of Hurricane Katrina (2005). *Mon. Wea. Rev.*, **137**, 3269–3293, doi: 10.1175/2009MWR2827.1.

Didlake, A. C., Jr. and R. A. Houze, Jr., 2013a: Convective-scale variations in the inner-core rainbands of a tropical cyclone. *J. Atmos. Sci.*, **70**, 504–523, doi: 10.1175/JAS-D-12-0134.1.

Didlake, A. C., Jr. and R. A. Houze, Jr., 2013b: Dynamics of the stratiform sector of a tropical cyclone rainband. *J. Atmos. Sci.*, **70**, 1891–1911, doi: 10.1175/JAS-D-12-0245.1.

Dunion, J. P., 2011: Rewriting the climatology of the Tropical North Atlantic and Caribbean Sea atmosphere. *J. Climate*, **24**, 893–908, doi: 10.1175/2010JCLI3496.1.

Fudeyasu, H. and Y. Wang, 2011: Balanced contribution to the intensification of a tropical cyclone simulated in TCM4: outer-core spinup process. *J. Atmos. Sci.*, **68**, 430–449, doi: 10.1175/2010JAS3523.1.

Hence, D. A. and R. A. Houze, Jr., 2008: Kinematic structure of convective-scale elements in the rainbands of Hurricanes Katrina and Rita (2005). *J. Geophys. Res.*, **113**, D15 108, doi: 10.1029/2007JD009429.

Hence, D. A. and R. A. Houze, Jr., 2012: Vertical structure of tropical cyclone rainbands as seen by the TRMM precipitation radar. *J. Atmos. Sci.*, **69**, 2644–2661, doi: 10.1175/JAS-D-11-0323.1.

Hildebrand, P. H. et al., 1996: The ELDORA/ASTRAIA airborne Doppler weather radar: high-resolution observations from TOGA COARE. *Bull. Amer. Meteor. Soc.*, **77**, 213–232, doi: 10.1175/1520-0477(1996)077<0213:TEADWR>2.0.CO;2.

Houze, R. A., Jr., 1997: Stratiform precipitation in regions of convection: a meteorological paradox? *Bull. Amer. Meteor. Soc.*, **78**, 2179–2196, doi: 10.1175/1520-0477(1997)078<2179:SPIROC>2.0.CO;2.

Houze, R. A., Jr., 2010: Review: clouds in tropical cyclones. *Mon. Wea. Rev.*, **138**, 293–344, doi: 10.1175/2009MWR2989.1.

Houze, R. A., Jr. et al., 2006: The hurricane rainband and intensity change experiment: observations and modeling of hurricanes Katrina, Ophelia, and Rita. *Bull. Amer. Meteor. Soc.*, **87**, 1503–1521, doi: 10.1175/BAMS-87-11-1503.

Jarvinen, B. R., C. J. Neumann, and M. A. S. Davis, 1984: A tropical cyclone data tape for the North Atlantic basin, 1886–1983: contents, limitations, and uses. NOAA Tech. Memo. NWS/NHC 22, NOAA/National Hurricane Center, 21 pp., Miami, FL.

Jorgensen, D. P., T. Matejka, and J. D. DuGranrut, 1996: Multi-beam techniques for deriving wind fields from airborne Doppler radars. *Meteor. Atmos. Phys.*, **59**, 83–104, doi: 10.1007/BF01032002.

Landsea, C. W. and J. L. Franklin, 2013: Atlantic hurricane database uncertainty and presentation of a new database format. *Mon. Wea. Rev.*, **141**, 3576–3592, doi: 10.1175/MWR-D-12-00254.1.

McAdie, C. J., C. W. Landsea, C. J. Neumann, J. E. David, E. S. Blake, and G. R. Hammer, 2009: *Tropical cyclones of the North Atlantic Ocean, 1951–2006 (6th Ed.)*. Historical Climatology Series, No. 6-2, National Climatic Data Center, 238 pp.

Montgomery, M. T. and R. J. Kallenbach, 1997: A theory for vortex Rossby-waves and its application to spiral bands and intensity changes in hurricanes. *Quart. J. Roy. Meteor. Soc.*, **123**, 435–465, doi: 10.1002/qj.49712353810.

Moon, Y. and D. S. Nolan, 2010: The dynamic response of the hurricane wind field to spiral rainband heating. *J. Atmos. Sci.*, **67**, 1779–1805, doi: 10.1175/2010JAS3171.1.

Samsury, C. E. and E. J. Zipser, 1995: Secondary wind maxima in hurricanes: airflow and relationship to rainbands. *Mon. Wea. Rev.*, **123**, 3502–3517, doi: 10.1175/1520-0493(1995)123<3502:SWMIHA>2.0.CO;2.

Sitkowski, M., J. P. Kossin, and C. M. Rozoff, 2011: Intensity and structure changes during hurricane eyewall replacement cycles. *Mon. Wea. Rev.*, **139**, 3829–3847, doi: 10.1175/MWR-D-11-00034.1.

Smith, R. K., M. T. Montgomery, and V. S. Nguyen, 2009: Tropical cyclone spin-up revisited. *Quart. J. Roy. Meteor. Soc.*, **135**, 1321–1335, doi: 10.1002/qj.428.

Testud, J., P. H. Hildebrand, and W.-C. Lee, 1995: A procedure to correct airborne Doppler radar data for navigation errors using the echo returned from the earth's surface. *J. Atmos. Oceanic Technol.*, **12**, 800–820, doi: 10.1175/1520-0426(1995)012<0800:APTCAD>2.0.CO;2.

Vigh, J. L., 2015: VDM+: The Enhanced Vortex Data Message Dataset (Version 1.100). Tropical Cyclone Data Project, National Center for Atmospheric Research, Research Applications Laboratory, Boulder, Colorado., [Available online at: http://dx.doi.org/10.5065/D61Z42GH.] Accessed 21 February 2017.

Vigh, J. L., et al., 2016: FLIGHT+: The Extended Flight Level Dataset for Tropical Cyclones (Version 1.1). Tropical Cyclone Data Project, National Center for Atmospheric Research, Research Applications Laboratory, Boulder, Colorado., [Available online at: http://dx.doi.org/10.5065/D6WS8R93.] Accessed 30 November 2016.

Willoughby, H. E., F. D. Marks, Jr., and R. J. Feinberg, 1984: Stationary and moving convective bands in hurricanes. *J. Atmos. Sci.*, **41**, 3189–3211, doi: 10.1175/1520-0469(1984)041<3189:SAMCBI>2.0.CO;2.

Yuter, S. E. and R. A. Houze, Jr., 1995: Three-dimensional kinematic and microphysical evolution of Florida cumulonimbus. Part II: frequency distributions of vertical velocity, reflectivity, and differential reflectivity. *Mon. Wea. Rev.*, **123**, 1941–1963, doi: 10.1175/1520-0493(1995)123<1941:TDKAME>2.0.CO;2.